

LONG-TERM ANALYTICAL PROPAGATION OF SATELLITE RELATIVE MOTION IN PERTURBED ORBITS

Tommaso Guffanti*, Simone D’Amico[†] and Michèle Lavagna[‡]

Many scientific applications require the implementation of satellite formation-flying in various orbits both around Earth and other planetary bodies. The design and guidance of these new formations call for relative dynamics models able to accurately and efficiently incorporate secular and long-periodic effects of all relevant perturbations. This paper leverages a quasi-nonsingular relative orbital elements state representation to devise a general methodology to model both conservative and non-conservative effects on the satellite relative motion in arbitrary eccentric orbits. By augmenting the state with force model parameters and Taylor expanding the time derivative to first order in mean space, three new plant matrices capturing the effects of solar radiation pressure, Sun and Moon third-body, and geopotential zonal harmonics up to third-order are formalized. In addition, two new effects have been discovered and modeled analytically in closed form. The first is the solar radiation pressure effect on the relative eccentricity vector of formations in near-circular orbit. The second is the lunisolar third-body effect on the relative inclination vector of formations in near-circular near-equatorial orbit. The new models are validated using numerical integration. Their accuracy and computational efficiency, combined with the novel analytical insight, can be leveraged for innovative relative orbit design and guidance.

INTRODUCTION

This paper responds to the need of modeling and comprehending the effects that natural perturbations have on the satellite relative motion in arbitrary orbital regimes. It focuses on solar radiation pressure (SRP), Sun and Moon third-body, and second and third-order zonal harmonics of the geopotential (J_2 and J_3). SRP and lunisolar third-body effects on the relative motion are often neglected by the current literature. This is due to the fact that they become significant in orbital regimes in which formation-flying has not been implemented yet. Nevertheless, future applications will extend the formation-flying implementation scenarios, requiring the modeling also of these perturbations.

To date, satellite formation-flying has been mainly implemented in low Earth orbit (LEO) by the missions GRACE,¹ TanDEM-X² and PRISMA.³ Moreover, NASA recently launched the Magnetospheric Multiscale (MMS) mission,⁴ which includes a formation of four satellites in an elliptical orbit. However, the variety of scientific applications and the mission costs reduction due to the intrinsic adaptability to satellite miniaturization make of great interest the application of formation-flying to new orbital scenarios using smaller space buses. The most relevant examples are proposed future missions around Earth as the ESA’s PROBA-3,⁵ the Space Rendezvous Laboratory’s (SLAB) Miniaturized Distributed Occulter/Telescope (mDOT),⁶ on-orbit servicing applications in geostationary orbit (GEO) and others.⁷ In addition, a couple of miniaturized low-mass low-power demanding spacecraft equipped with a synthetic aperture radar can be exploited for bi-static mapping other planets or moons of the Solar System (e.g. Saturn’s moon Titan).⁸ The orbital perturbations that would affect the satellite relative motion in high or highly elliptical orbits around Earth or around other planets are of various types (e.g. geopotential, third-body and SRP) and magnitude (e.g. mapping a planet closer to the Sun or a moon orbiting around a very massive central attractor). As a consequence, in order to

*Ph.D. Candidate, Aeronautics and Astronautics, Stanford University, 496 Lomita Mall, Stanford, CA 94305.

[†] Assistant Professor, Aeronautics and Astronautics, Stanford University, 496 Lomita Mall, Stanford, CA 94305.

[‡] Associate Professor, Department of Aerospace Science and Technology, Politecnico di Milano, via La Masa 34, 20156, Milan, Italy.

design and guide the future formation-flying missions, more comprehensive relative motion dynamic models are necessary. These models have to include all the relevant perturbations, while providing the propagation accuracy and computational efficiency required by the on-board resources available on the miniaturized buses. In addition, a more extensive understanding of how all the different types of perturbations affect the satellite relative motion is needed in order to exploit at the maximum the perturbing environment and reduce the control mass required in orbit. In this sense, analytical models can be leveraged for mission design optimization.

Linear dynamic models of the satellite relative motion affected by orbital perturbations are well known in literature and have been extensively exploited in real space missions application scenarios. Using a Cartesian representation of the relative motion, Schweighart and Izzo^{9,10} expand on the Hill-Clohessy-Wiltshire model for formation in unperturbed near-circular orbit,¹¹ by including first-order secular effects of J_2 and differential drag. The Yamanaka-Ankersen model¹² for linear propagation of the relative position and velocity in eccentric orbits instead does not include perturbations. The inclusion of perturbations is simplified by the use of a relative state with components that are non-linear combinations of the Keplerian orbital elements of the two spacecraft in formation, which hereafter are called Relative Orbital Elements (ROE). This state varies slowly with time and allows the use of astrodynamics tools such as the Lagrange and Gauss variation of parameters (VOP) form of the equations of motion¹³ to be leveraged to include perturbations. To date, the literature that exploits this state representation mainly focused on the inclusion of the effects of J_2 and differential drag which are the more relevant in the orbital regimes of the currently launched or planned formation-flying missions. In particular, contributions can be divided in two general tracks. The first one originates from the work of Gim and Alfrend which formalized a State Transition Matrix (STM) including first-order secular and osculating J_2 effects on the relative motion in arbitrary eccentric orbit.¹⁴ This STM was used in the design process for NASA's MMS mission¹⁵ and in the maneuver-planning algorithm of NASA's CPOD mission.¹⁶ A similar STM was later derived for a fully nonsingular ROE state¹⁷ and more recent works have included higher-order zonal geopotential harmonics.^{18,19} However, this approach has not yet produced an STM including non-conservative perturbations. Meanwhile, researcher at SLAB and collaborators have worked independently to develop models using a different ROE state. Specifically, D'Amico derived an STM which captures the first-order secular effects of J_2 on formations in near-circular orbits²⁰ in his thesis. This model has since been expanded by Gaias et al.^{21,22} to include the effect of time-varying differential drag on the relative semi-major axis and on the relative eccentricity vector. This state formulation was first used in flight to plan the GRACE formation's longitude swap maneuver²³ and has since found application in the guidance, navigation, and control (GN&C) systems of the TanDEM-X²⁴ and PRISMA³ missions as well as the AVANTI experiment.²⁵ More recent work of Koenig and the first two authors of this paper²⁶ presents STM including both first-order secular J_2 effects and differential drag in orbit of arbitrary eccentricity for three different ROE representations, extending and harmonizing the previously mentioned works of Gaias et al.²² and Gim-Alfrend.^{14,17} Attempts to model the effects of Sun and Moon third-body and SRP also exist in literature. Regarding the third-body, Roscoe et al.²⁷ exploited the double-averaged equations of the lunar gravitational perturbation for modeling its effects on the differential Keplerian elements. Spiridonova et al.^{28,29} focused on the on-orbit servicing scenario in GEO and modeled the effects of SRP and Sun and Moon third-body on the quasi-nonsingular ROE for a formation in near-GEO. The SRP in particular is modeled in the Cartesian Earth-Centered-Inertial (ECI) frame as a differential perturbing acceleration purely dependent on the ballistic coefficient difference between the satellites and subsequently applied to the ROE state through linear maps. A more comprehensive survey of spacecraft relative motion dynamics models is presented by Sullivan et al.³⁰

What the current literature does not provide is a general methodology able to include both conservative and non-conservative perturbing effects on the relative motion in arbitrary eccentric orbit. Following the research track started by D'Amico in his thesis,²⁰ this paper contributes to the state-of-the-art by formalizing this general methodology. More in detail, a first-order Taylor expansion of the time derivative of the ROE state augmented by the satellites ballistic coefficient differences is performed to formalize plant matrices that link the quasi-nonsingular ROE state with its variation including both conservative and non-conservative perturbations. In particular, the paper presents three new plant matrices that model the effects of SRP, Sun and Moon third-body and geopotential zonal harmonics up to third-order on the quasi-nonsingular ROE. The in-

clusion of the considered perturbations is permitted by leveraging the formulations of Liu and Alford^{31,32} and Cook,³³ which express the mean orbital elements variations due to J_2 and J_3 effects and lunisolar effects correspondingly. The use of mean elements, obtained by averaging over the satellite orbit the short-period oscillations, finds fruitful application in relative motion propagation due to the fact that the short-period variations cancel-out largely when differentiating the absolute states. Differential drag can also be handled but it is not here further analyzed considering the extensive work presented by Gaias et al.²² and Koenig et al.²⁶ The analytical insight provided by the new linear models is exploited to get information on the ROE variation under the analyzed perturbations. In particular, from the SRP and third-body plant matrices, two new reduced models are extracted which retain the most significant effects of the two perturbations on the ROE. Integrating in time, a circulation of the relative eccentricity vector in its phase space for formations in near-circular orbit due to SRP, and a rotation of the relative inclination vector of formation in near-circular near-equatorial orbit due to Sun and Moon third-body, are discovered and modeled analytically. Finally, the new dynamic models are validated with respect to numerical integration of the equations of motion with perturbations, and their accuracy and computational efficiency is assessed.

STATE DEFINITION

Consider without loss of generality a formation composed by two satellites, a chief and a deputy. The chief satellite is taken as the reference of the formation. In the ECI reference frame the set of quasi-nonsingular chief orbital elements is χ . The relative motion of the deputy satellite with respect to the chief can be parametrized through a set of quasi-nonsingular Relative Orbital Elements (ROE),²⁰ $\delta\chi$, which are a non-linear combination of the absolute orbital elements

$$\chi = \begin{pmatrix} a \\ u \\ e_x \\ e_y \\ i \\ \Omega \end{pmatrix} = \begin{pmatrix} a \\ \omega + M \\ e \cos(\omega) \\ e \sin(\omega) \\ i \\ \Omega \end{pmatrix} \quad (1) \quad \delta\chi = \begin{pmatrix} \delta a \\ \delta\lambda \\ \delta e_x \\ \delta e_y \\ \delta i_x \\ \delta i_y \end{pmatrix} = \begin{pmatrix} (a_d - a)/a \\ (u_d - u) + (\Omega_d - \Omega) \cos(i) \\ e_{x,d} - e_x \\ e_{y,d} - e_y \\ i_d - i \\ (\Omega_d - \Omega) \sin(i) \end{pmatrix} \quad (2)$$

where $e = (e_x, e_y)^t$ is the eccentricity vector and $u = \omega + M$ is the mean argument of latitude. The subscript "d" is introduced to denote quantities related to the deputy satellite. The semi-major axis difference, δa , has been normalized through the chief semi-major axis to have dimensionless quantity. $\delta\lambda$ is the relative mean longitude between the satellites. The other four terms define the relative eccentricity and relative inclination vectors, which in polar coordinates are

$$\delta e = \begin{pmatrix} \delta e_x \\ \delta e_y \end{pmatrix} = \delta e \begin{pmatrix} \cos \varphi \\ \sin \varphi \end{pmatrix} \quad \delta i = \begin{pmatrix} \delta i_x \\ \delta i_y \end{pmatrix} = \delta i \begin{pmatrix} \cos \theta \\ \sin \theta \end{pmatrix} \quad (3)$$

The norms of the two vectors δe and δi have not to be confused with the arithmetic differences of eccentricities and inclinations of the deputy and chief orbits. The phase angles of the two vectors φ and θ are termed the relative perigee and relative ascending node respectively, but they do not equal the arithmetic differences of the corresponding angles. The general linearized relative motion of the deputy satellite relative to the chief for arbitrary eccentricities in a Keplerian two-body problem is provided in terms of ROE as

$$\delta\lambda(t) = -1.5n(t - t_0)\delta a_0 + \delta\lambda_0 \quad (4)$$

Where n is the chief mean angular motion, and the subscript "0" indicates the quantities at initial time.

REVIEW OF PERTURBED ABSOLUTE DYNAMICS

The analytical expansion method to solve the equations of motion with perturbations is based on the derivation of averaged equations of motion in mean orbital elements.^{13,34} Such method usually relies on the analytical series expansion of the perturbing accelerations or disturbing potential functions, which are then truncated and inserted in the Lagrange or Gauss VOP. The resulting expressions are then integrated over one orbital

period to isolate the secular and long-periodic terms, averaging out the short-periodic ones. The fundamental averaging equation is

$$\langle \dot{\chi}_j \rangle = \frac{1}{2\pi} \int_0^{2\pi} \dot{\chi}_j dM \quad (5)$$

where $\langle \dot{\chi}_j \rangle$ is the averaged equation of an orbital element χ_j that is perturbed by a disturbing force. A wide literature about these models exists. This paper focuses on two specific works, the one of Liu and Alford^{31,32} for the second and third-order zonal harmonics of the geopotential (J_2 and J_3) and the one of Cook³³ for the lunisolar perturbations. The analytical formulations of these models are reported in Appendix A. A detailed description of the models underlying hypotheses is presented in the following, together with the few simplification assumptions considered in order to derive the plant matrices. All the most significant effects are included in the plant matrices, as will be verified later in the paper comparing with the numerical propagator.

Regarding the geopotential perturbation, Liu and Alford provides the rates of variation of the six mean orbital elements due to the zonal harmonics J_2 and J_3 . They include the first-order secular drifts of the right ascension of ascending node (RAAN, Ω), argument of perigee (ω) and mean anomaly (M), induced by the even zonal harmonic J_2 , and the long-periodic variations induced by J_3 on e , i , Ω , ω and M . Their model has no limitation in orbit eccentricity, but becomes singular for the circular case in the J_3 terms of ω and M and for the zero inclination case in the J_3 terms of Ω and ω . The variations in ω and M tend to cancel and therefore the argument of latitude is almost not affected by J_3 , in particular when the orbit is nearly circular.³⁴ The effect of J_3 on u has been neglected during the J_3 plant matrix derivation.

Regarding the Sun and Moon third-body perturbation, Cook inserts the disturbing potential (limited to the second term in the Legendre polynomial expansion) of a third-body in circular orbit in the Lagrange VOP neglecting the high-order terms in r/r_3 , where r and r_3 are the radial distance from the Earth of the satellite and disturbing body respectively. As next step, he averages over the satellite orbital period providing the rates of change of the mean orbital elements including both secular and long-periodic effects. His model has no limitations in orbit eccentricity, but becomes singular for the zero inclination case in the terms of Ω and ω . Moreover, the model decreases in accuracy with increasing r/r_3 , therefore it can be reasonably applied to orbits with semi-major axis not exceeding one tenth of the Moon's distance from the Earth. In addition, considering that the mean motion of the disturbing body is much smaller than the satellite one, the third-body is hypothesized fixed within each averaging period. Analyzing more in detail the effects on the orbital parameters, the only secular changes induced by third-body are in Ω and ω . Long-periodic effects are instead present in i , Ω , e and ω . In Appendix A and in the third-body plant matrix derivation, both the secular and long-periodic rates of change in i and Ω are considered. Whereas, only the secular variation of ω related to the Ω drift is included, neglecting long-periodic effects on e and ω themselves. No expression for the fast variable under the third-body action is provided, which is therefore considered in the following as expressed in Appendix A.

Regarding the SRP perturbation, Cook inserts the radial, transverse and normal components of the disturbing force evaluated at the perigee as if the perigee is in Sun-light in the VOP equations. Then, neglecting the effect of eclipses, he averages over the satellite orbital period providing the rates of change of the mean orbital elements. His model has no limitations in orbit eccentricity, but becomes singular for the circular case in the term of ω and for the zero inclination case in the terms of Ω , ω and M . SRP induces long-periodic variations in all orbital elements, with the most significant on e and ω . The period of the variations is related to the motion of the Earth about the Sun, so it can be as long as a year. The net effect on the semi-major axis, for an orbit entirely in Sun-light is zero. The SRP disturbance is proportional to the ballistic coefficient (B_{srp}) of the spacecraft, therefore, more and more relevant as much the spacecraft's mass is lower and the surface area is large and reflective.

These analytical dynamic models permit to propagate the secular/long-periodic variations in time of the mean orbital elements with an interesting trade-off of propagation accuracy and computational efficiency, as will be highlighted comparing with the numerical propagator. Moreover, the analytical expressions provide useful insight on the absolute perturbed motion geometry which can be leveraged for various purposes as orbit design. In the following of the paper, these qualities are applied and extended to the propagation and analysis of the relative perturbed motion.

PLANT MATRIX DERIVATION METHODOLOGY

The objective is to formulate a plant matrix, A_p , for relative motion propagation, including all the considered perturbations exploiting the analytical models introduced in the previous section. From Eq. 2, the derivative in time of the ROE state is given by

$$\dot{\delta\chi} = \begin{pmatrix} \dot{\delta a} \\ \dot{\delta \lambda} \\ \dot{\delta e_x} \\ \dot{\delta e_y} \\ \dot{\delta i_x} \\ \dot{\delta i_y} \end{pmatrix} = \begin{pmatrix} (a_d - \dot{a})/a - \dot{a}\delta a/a \\ (u_d - \dot{u}) + (\dot{\Omega}_d - \dot{\Omega}) \cos(i) - (\dot{i})\delta i_y \\ e_{x_d} - \dot{e}_x \\ e_{y_d} - \dot{e}_y \\ (i_d) - (\dot{i}) \\ (\dot{\Omega}_d - \dot{\Omega}) \sin(i) + (\dot{i})\delta i_y / \tan(i) \end{pmatrix} \quad (6)$$

In general, the perturbations that cause a variation of the orbital elements are of two types, conservative and non-conservative. In the first case, the differential perturbing effect on two satellites in formation depends on the orbit geometrical differences, $\dot{\delta\chi}(\delta\chi)$. In the second case, the differential perturbing effect depends also on the difference between satellites features, represented as ballistic coefficient difference, $\dot{\delta\chi}(\delta\chi, \Delta B)$. In order to formalize the plant matrix, it is necessary to make these relations explicit and linearize them.

Firstly, the deputy satellite orbital elements can be expressed as a function of the chief ones and of the ROE, $\chi_d = \chi_d(\chi, \delta\chi)$,

$$\begin{aligned} a_d &= a(1 + \delta a), & e_{x_d} &= e_x + \delta e_x, & e_{y_d} &= e_y + \delta e_y, & i_d &= i + \delta i_x, \\ \Omega_d &= \Omega + \delta i_y / \sin(i), & u_d &= u - \delta i_y / \tan(i) + \delta \lambda. \end{aligned} \quad (7)$$

Secondly, the deputy satellite ballistic coefficient can be linked to the one of the chief and to the ballistic coefficient difference

$$B_d = B + \Delta B. \quad (8)$$

B is the generic ballistic coefficient, and can be related either to the SRP or to the atmospheric drag. Finally, the dependence of the state variation from the state itself and the ballistic coefficient difference can be expressed explicitly as

$$\dot{\delta\chi} = \begin{pmatrix} (a_d(\delta\chi, \Delta B) - \dot{a})/a - \dot{a}\delta a/a \\ (u_d(\delta\chi, \Delta B) - \dot{u}) + (\dot{\Omega}_d(\delta\chi, \Delta B) - \dot{\Omega}) \cos(i) - (\dot{i})\delta i_y \\ e_{x_d}(\delta\chi, \Delta B) - \dot{e}_x \\ e_{y_d}(\delta\chi, \Delta B) - \dot{e}_y \\ (i_d)(\delta\chi, \Delta B) - (\dot{i}) \\ (\dot{\Omega}_d(\delta\chi, \Delta B) - \dot{\Omega}) \sin(i) + (\dot{i})\delta i_y / \tan(i) \end{pmatrix} \quad (9)$$

This relation can be linearized. Taylor expanding $\dot{\delta\chi}$ to the first-order in the neighborhood of $\delta\chi = \mathbf{0}$ provides

$$\dot{\delta\chi}(\delta\chi, \Delta B) = \dot{\delta\chi}(\mathbf{0}, \Delta B) + \left. \frac{\partial \dot{\delta\chi}}{\partial \delta\chi} \right|_{\delta\chi=\mathbf{0}} \cdot (\delta\chi - \mathbf{0}) \quad (10)$$

The term $\dot{\delta\chi}(\mathbf{0}, \Delta B)$ is different from zero if any difference in ballistic coefficient between deputy and chief satellites is present. Nevertheless, the relation that links the ballistic coefficient difference with the state variation is linear, therefore it is possible to define a new state $\delta\tilde{\chi} = [\delta\chi^t, \Delta B]^t$ for which the previous expansion becomes

$$\dot{\delta\tilde{\chi}}(\delta\tilde{\chi}) = \left. \frac{\partial \dot{\delta\tilde{\chi}}}{\partial \delta\tilde{\chi}} \right|_{\delta\tilde{\chi}=\mathbf{0}} \cdot \delta\tilde{\chi} \quad (11)$$

where

$$\left. \frac{\partial \dot{\tilde{\chi}}}{\partial \tilde{\chi}} \right|_{\tilde{\chi}=\mathbf{0}} = \left[\begin{array}{ccccccc} \frac{\partial \dot{\tilde{\chi}}}{\partial \delta a} & \frac{\partial \dot{\tilde{\chi}}}{\partial \delta \lambda} & \frac{\partial \dot{\tilde{\chi}}}{\partial \delta e_x} & \frac{\partial \dot{\tilde{\chi}}}{\partial \delta e_y} & \frac{\partial \dot{\tilde{\chi}}}{\partial \delta i_x} & \frac{\partial \dot{\tilde{\chi}}}{\partial \delta i_y} & \frac{\partial \dot{\tilde{\chi}}}{\partial \Delta B} \end{array} \right] \Big|_{\tilde{\chi}=\mathbf{0}} \quad (12)$$

ΔB is the generic ballistic coefficient difference and can be related either to the SRP or to the atmospheric drag. In case of differential drag, Koenig et al.²⁶ propose also a different approach by incrementing the relative state by the relative semi-major axis and eccentricity vector components time variations, obtaining very good performances. Eq. 12 represents the general plant matrix, with size $[7 \times 7]$. The upper left $[6 \times 6]$ block contains the terms that relate the ROE with their variations and will be filled by the conservative perturbing effects (geopotential and third-body) and by that contribution of the non-conservative perturbing effects (e.g. SRP) that only depends on the orbital geometrical differences (considering equal ballistic coefficients). The upper right $[6 \times 1]$ column will instead contain the linear relations that exist in between the ROE variations and the ballistic coefficient difference and will be filled only by the non-conservative perturbing effects. By taking into account the dependence of the different terms in $\delta \tilde{\chi}$ from the ROE and from the ballistic coefficient difference, the seven columns of the plant matrix can be expressed in a compact form as

$$\left. \frac{\partial \dot{\tilde{\chi}}}{\partial \tilde{\chi}} \right|_{\tilde{\chi}=\mathbf{0}} = \left[\begin{array}{c} \frac{\partial \dot{a}_d}{\partial \delta \tilde{\chi}} \Big|_{\tilde{\chi}=\mathbf{0}} / a - \frac{\dot{a}}{a} \delta_j^1 \\ \frac{\partial \dot{u}_d}{\partial \delta \tilde{\chi}} \Big|_{\tilde{\chi}=\mathbf{0}} + \frac{\partial \dot{\Omega}_d}{\partial \delta \tilde{\chi}} \Big|_{\tilde{\chi}=\mathbf{0}} \cos(i) - (\dot{i}) \delta_j^6 \\ \frac{\partial \dot{e}_{x_d}}{\partial \delta \tilde{\chi}} \Big|_{\tilde{\chi}=\mathbf{0}} \\ \frac{\partial \dot{e}_{y_d}}{\partial \delta \tilde{\chi}} \Big|_{\tilde{\chi}=\mathbf{0}} \\ \frac{\partial (\dot{i}_d)}{\partial \delta \tilde{\chi}} \Big|_{\tilde{\chi}=\mathbf{0}} \\ \frac{\partial \dot{\Omega}_d}{\partial \delta \tilde{\chi}} \Big|_{\tilde{\chi}=\mathbf{0}} \sin(i) + (\dot{i}) / \tan(i) \delta_j^6 \\ 0 \end{array} \right] \quad (13)$$

where δ_j^i , for $j = 1, \dots, 7$, is the Kronecker delta. The equations in Appendix A for the deputy and chief satellites, reformulated in terms of quasi-nonsingular orbital elements, are substituted in $\frac{\partial \dot{a}_d}{\partial \delta \tilde{\chi}} \Big|_{\tilde{\chi}=\mathbf{0}}$, $\frac{\partial \dot{u}_d}{\partial \delta \tilde{\chi}} \Big|_{\tilde{\chi}=\mathbf{0}}$, $\frac{\partial \dot{e}_{x_d}}{\partial \delta \tilde{\chi}} \Big|_{\tilde{\chi}=\mathbf{0}}$, $\frac{\partial \dot{e}_{y_d}}{\partial \delta \tilde{\chi}} \Big|_{\tilde{\chi}=\mathbf{0}}$, $\frac{\partial (\dot{i}_d)}{\partial \delta \tilde{\chi}} \Big|_{\tilde{\chi}=\mathbf{0}}$, $\frac{\partial \dot{\Omega}_d}{\partial \delta \tilde{\chi}} \Big|_{\tilde{\chi}=\mathbf{0}}$, \dot{a} and (\dot{i}) . Subsequently, by calculating the partial derivatives, the plant matrices related to each considered perturbing effect are formalized. Finally, considering that the models in Appendix A are independent from one another (i.e. the formulations for geopotential, third-body, SRP are distinct), it is possible to apply the superposition principle for each orbital parameter variation and write for the full state

$$\mathbf{A}_p = \left. \frac{\partial \dot{\tilde{\chi}}}{\partial \tilde{\chi}} \right|_{\tilde{\chi}=\mathbf{0}} = \mathbf{A}_{geop} + \mathbf{A}_{3rdb} + \mathbf{A}_{srp} = \left. \frac{\partial \dot{\tilde{\chi}}_{geop}}{\partial \delta \tilde{\chi}} \right|_{\tilde{\chi}=\mathbf{0}} + \left. \frac{\partial \dot{\tilde{\chi}}_{3rdb}}{\partial \delta \tilde{\chi}} \right|_{\tilde{\chi}=\mathbf{0}} + \left. \frac{\partial \dot{\tilde{\chi}}_{srp}}{\partial \delta \tilde{\chi}} \right|_{\tilde{\chi}=\mathbf{0}} \quad (14)$$

By defining the complete plant matrix \mathbf{A} that maps the state vector in its variation as superposition of the Keplerian and perturbative contribution the state equation becomes

$$\dot{\tilde{\chi}} = \mathbf{A} \cdot \delta \tilde{\chi} = (\mathbf{A}_{Kepl.} + \mathbf{A}_p) \cdot \delta \tilde{\chi} \quad (15)$$

where $\mathbf{A}_{Kepl.}$ is obtained by substituting the time derivative of Eq. 4 in Eq. 12. The range of applicability of the linear model just formalized can be assessed by looking at the second-order terms truncated by the first-order Taylor expansion

$$\dot{\tilde{\chi}}(\delta \tilde{\chi}) = \left. \frac{\partial \dot{\tilde{\chi}}}{\partial \delta \tilde{\chi}} \right|_{\tilde{\chi}=\mathbf{0}} \cdot \delta \tilde{\chi} + \frac{1}{2} \sum_{j=1}^7 \sum_{i=1}^7 \left. \frac{\partial^2 \dot{\tilde{\chi}}}{\partial \delta \tilde{\chi}_j \partial \delta \tilde{\chi}_i} \right|_{\tilde{\chi}=\mathbf{0}} \cdot \delta \tilde{\chi}_j \delta \tilde{\chi}_i \quad (16)$$

The truncated terms contain both square and mixed products of the state elements. Considering that the linearization is effectuated in the neighborhood of $\delta\chi = \mathbf{0}$, it holds for small ROE. The relation that links $\delta\dot{\chi}$ with ΔB is linear, therefore the second order partial derivative $\left. \frac{\partial^2 \delta\dot{\chi}}{\partial^2 \Delta B} \right|_{\delta\dot{\chi}=\mathbf{0}}$ is zero and no terms containing ΔB^2 are present. The linear model is therefore valid for arbitrary large ballistic coefficient difference as long as the ROE are small and guarantee small mixed products $\delta\tilde{\chi}_j \Delta B$ (for $j = 1, \dots, 6$). In addition, the equations in Appendix A are averaged over the satellite orbit, therefore they don't depend from the fast variable and the plant matrix column $\left. \frac{\partial \delta\tilde{\chi}}{\partial \delta\lambda} \right|_{\delta\dot{\chi}=\mathbf{0}}$ is zero. Avoiding the linearization with respect to $\delta\lambda$ implies the validity of the linear model also in case of big relative mean longitude, which is important considering its linear increase in case of not null initial condition on the relative mean semi-major axis. Anyway, the previous approach is general and if equations that include also short-periodic terms are considered, they will determine a second column different from zero. In this case, the linear model would be valid only for small $\delta\lambda$ that guarantees small truncation errors proportional to $\delta\lambda\delta\tilde{\chi}_j$ (for $j = 1, \dots, 7$).

LINEARIZED PERTURBED RELATIVE DYNAMICS

Following the methodology explained in the previous section, the plant matrices for J_2 , J_3 , Sun and Moon third-body and SRP have been computed and are reported in Appendix B. The plant matrix for J_2 is consistent to the one obtained by Koenig et al.²⁶ The other three have been newly derived. By looking at the null matrices' rows, it is possible to individuate the ROE that are unaffected by a specific perturbing effect. The range of applicability of each linear model is instead assessed by looking at the second-order terms truncated by the first-order Taylor expansion. The results are summarized in Tab. 1. In particular, J_2 affects all ROE

Table 1: Affected ROE and required small state elements for linearization validity.

	Affected ROE						Required small state elements						
	δa	$\delta\lambda$	δe_x	δe_y	δi_x	δi_y	δa	$\delta\lambda$	δe_x	δe_y	δi_x	δi_y	ΔB
J_2		X	X	X		X	X		X	X	X		
J_3		X	X	X	X	X	X		X	X	X		
TB		X	X	X	X	X	X		X	X	X	X	
SRP		X	X	X	X	X	X		X	X	X	X	

with the exception of δa and δi_x , in consistency with the literature.²⁰ Sun and Moon third-body, SRP and J_3 affect all ROE with the exception of δa . Regarding the ranges of applicability of the linear models, J_2 and J_3 plant matrices are valid for small separations in δa , δe_x , δe_y and δi_x but arbitrarily large separations in $\delta\lambda$ and δi_y . Sun and Moon third-body and SRP plant matrices instead are valid for small separations in all the ROE with the only exception of $\delta\lambda$. For SRP in addition, the linearization with respect to ΔB imposes no constraints on its magnitude as long as $\delta\tilde{\chi}_j$ (for $j = 1, 3, \dots, 6$) are small. All the plant matrices in Appendix B are time-variant. The time dependency relations are summarized in Tab. 2. Analyzing case by case, the

Table 2: Plant matrices time dependency.

	Time dependency							
	$a(t)$	$e(t)$	$\omega(t)$	$i(t)$	$\Omega(t)$	$\gamma_{Sun}(t)$	$\gamma_{Moon}(t)$	$B_{srp}(t)$
J_2			X					
J_3		X	X	X				
TB			X	X	X	X	X	
SRP		X	X	X	X	X		X

J_2 plant matrix time dependency is associated with the variation of the chief eccentricity vector components (e_x and e_y) related to the secular drift of ω . In this case, Koenig et al.²⁶ recover a time-invariant form by applying a simple rotation of the relative state of ω . The J_3 plant matrix varies in time due to the long-periodic

oscillations of e , i and ω . The third-body plant matrix contains chief parameters that vary on the long-period or secularly (i , Ω and ω), and the third-body ephemerides that vary in particular in the fast variable (u_3). Finally, the SRP plant matrix time dependency is associated with the long-periodic variations of e , i , Ω and ω , the variation of the Sun ecliptic longitude (λ_s), and the variation of the chief satellite illuminated area included in B_{srp} . For both J_3 , third-body and SRP plant matrices no direct intuitive linear transformation can be found to recover a time-invariant form. The formalized linear models have no limitation in orbit eccentricity and don't suffer of singularity in the circular case thanks to the reformulation of the equations in Appendix A in terms of quasi-nonsingular orbital elements prior to linearizing. Singularities in the zero inclination case remain instead in the J_3 , third-body and SRP plant matrices.

The total geopotential plant matrix is expressed as superposition of J_2 and J_3 plant matrices, as

$$\mathbf{A}_{geop}(\chi(t)) = \mathbf{A}_{geopJ_2}(\chi(t)) + \mathbf{A}_{geopJ_3}(\chi(t)) + \mathcal{O}(\delta\tilde{\chi}_j\delta\tilde{\chi}_i) \quad j/i = 1, 3, 4, 5 \quad (17)$$

The total third-body plant matrix is expressed superimposing the Sun and Moon third-body plant matrices, obtained by inserting the specific ephemerides, as

$$\mathbf{A}_{3^{rd}b}(\chi(t), \gamma_3(t)) = \mathbf{A}_{3^{rd}b_{Sun}}(\chi(t), \gamma_{Sun}(t)) + \mathbf{A}_{3^{rd}b_{Moon}}(\chi(t), \gamma_{Moon}(t)) + \mathcal{O}(\delta\tilde{\chi}_j\delta\tilde{\chi}_i) \quad j/i = 1, 3, \dots, 6 \quad (18)$$

The SRP plant matrix is instead

$$\mathbf{A}_{srp}(\chi(t), \lambda_s(t), B_{srp}(t)) = \mathbf{A}_{srp}(\chi(t), \lambda_s(t), B_{srp}(t)) + \mathcal{O}(\delta\tilde{\chi}_j\delta\tilde{\chi}_i) \quad j = 1, 3, \dots, 6 \quad i = 1, 3, \dots, 7 \quad (19)$$

Finally, by superimposing the previous matrices the complete perturbative plant matrix is

$$\mathbf{A}_p(t) = \mathbf{A}_p(\chi(t), \gamma_{Sun}(t), \gamma_{Moon}(t), B_{srp}(t)) = \mathbf{A}_{geop}(t) + \mathbf{A}_{3^{rd}b}(t) + \mathbf{A}_{srp}(t) + \mathcal{O}(\delta\tilde{\chi}_j\delta\tilde{\chi}_i) \quad j = 1, 3, \dots, 6 \quad i = 1, 3, \dots, 7 \quad (20)$$

The system expressed in Eq. 15 is therefore Linear Time Variant, since a constant Keplerian plant matrix is superimposed to a time varying perturbative plant matrix.

Relative Perturbed Motion Propagation

In order to propagate the motion using the formalized plant matrices, the state transition matrix (STM) that maps the state vector at time t_0 in the state vector at time t_f has to be formulated. Since the models are defined in a mean orbital elements space, within each orbital period the plant matrices time dependency is confined in the time varying Sun and Moon ephemerides and B_{srp} . Considering as approximation hypothesis both the Sun, the Moon and B_{srp} fixed within each chief satellite orbital period, the complete plant matrix becomes constant and the system in Eq. 15 becomes Linear Time Invariant in the interval. Therefore, for a time step $[t_i, t_{i+1}]$ such that $t_{i+1} - t_i = T_i$ (where T_i is the chief orbital period in the time interval considered), the STM that maps the state vector at time t_i ($\delta\tilde{\chi}(t_i)$) in the state vector at time t_{i+1} ($\delta\tilde{\chi}(t_{i+1})$) is

$$\Phi(t_{i+1}, t_i) = \mathbf{A}_i \cdot T_i + \mathbf{I} \quad (21)$$

where \mathbf{A}_i is computed using the chief mean orbital elements, the Sun and Moon ephemerides and B_{srp} at time t_i . \mathbf{I} is the identity matrix. The propagation from the initial condition to the final condition can therefore be built as

$$\delta\tilde{\chi}(t_f) = \Phi(t_f, t_0) \cdot \delta\tilde{\chi}(t_0) = \prod_{i=0}^{N-1} \Phi(t_{i+1}, t_i) \cdot \delta\tilde{\chi}(t_0) \quad (22)$$

with $N = \text{int}\left(\frac{t_f - t_0}{T}\right)$. At each step, the chief mean orbital elements, the Sun and Moon ephemerides and B_{srp} are updated. This approach can be simplified if the propagation is performed for a smaller time interval in which the time varying parameters don't change significantly, as

$$\delta\tilde{\chi}(t_f) = \Phi(t_f, t_0) \cdot \delta\tilde{\chi}(t_0) = [\mathbf{A}_0 \cdot (t_f - t_0) + \mathbf{I}] \cdot \delta\tilde{\chi}(t_0) \quad (23)$$

where \mathbf{A}_0 is computed at time t_0 .

Solar Radiation Pressure Reduced Model

It is of interest to isolate the most significant terms in the SRP plant matrix presented in Appendix B. This permits to obtain simplified expressions with a direct insight on the perturbed relative motion geometry, which can be leveraged for relative orbit design and guidance. Moreover, this will help giving an interpretation to the numerical validation of the model. The SRP plant matrix models the differential perturbing effect due to both orbit geometrical differences (upper-left $[6 \times 6]$ block) and ballistic coefficient difference (upper-right $[6 \times 1]$ column). Considering the distance between the satellites and the Sun, the two chief-Sun and deputy-Sun relative position vectors are almost coincident and the chief-deputy orbit geometrical differences seen by the Sun are very small. Therefore, the contribution related to the ballistic coefficient difference is predominant by order of magnitudes and can be isolated neglecting the rest, as assumed also in the model of Spiridonova.^{28,29} In addition, the most significant yearly-periodic variations induced by SRP are on e and ω . The two terms in the last column which model the effects on the relative eccentricity vector components due to a pure ballistic coefficient difference can therefore be extracted from the SRP plant matrix. Moreover, in order to further simplify the formulation, the hypothesis of near-circular chief orbit is introduced and the terms proportional to e^2 are neglected. The resulting rates of variation of the relative eccentricity vector components are

$$\begin{pmatrix} \delta \dot{e}_x \\ \delta \dot{e}_y \end{pmatrix} = \frac{3 F_{srp}}{2 \sqrt{\mu}} \sqrt{a} \Delta B \begin{pmatrix} c_{\epsilon/2}^2 c_i \sin(\Omega - \lambda_s(t)) + s_{\epsilon/2}^2 c_i \sin(\Omega + \lambda_s(t)) - s_{\epsilon} s_i \sin(\lambda_s(t)) \\ c_{\epsilon/2}^2 \cos(\Omega - \lambda_s(t)) + s_{\epsilon/2}^2 \cos(\Omega + \lambda_s(t)) \end{pmatrix} \quad (24)$$

where $F_{srp} = \frac{P_{Sun}}{c} \left(\frac{a_{Sun}}{r_{Sun}} \right)^2$, $\frac{P_{Sun}}{c} = \frac{1353 \text{ W/m}^2}{3 \cdot 10^8 \text{ m/s}}$, $\frac{a_{Sun}}{r_{Sun}} \approx 1$ or as in Chao,³⁴ $\epsilon = 23.44^\circ$, $\sin(\cdot) = s$ and $\cos(\cdot) = c$. Approximating the chief i and Ω as constant, the only time varying contribution is the Sun ecliptic longitude, $\lambda_s(t)$. As a first approximation, it can be modeled as an angle which linearly varies of 360° in one year with a law of variation as $\lambda_s(t) = n_s t + \lambda_{s,0}$, where $n_s = 2\pi/1y$. Given these approximations, Eq. 24 can be integrated exactly from t_0 to t , providing

$$\begin{pmatrix} \delta e_x(t) \\ \delta e_y(t) \end{pmatrix} = \begin{pmatrix} \delta e_{x,0} \\ \delta e_{y,0} \end{pmatrix} + \frac{3 F_{srp}}{2 \sqrt{\mu} n_s} \sqrt{a} \Delta B \cdot \begin{pmatrix} c_{\epsilon/2}^2 c_i [\cos(\lambda_s(t) - \Omega) - \cos(\lambda_{s,0} - \Omega)] - s_{\epsilon/2}^2 c_i [\cos(\lambda_s(t) + \Omega) - \cos(\lambda_{s,0} + \Omega)] + s_{\epsilon} s_i [\cos(\lambda_s(t)) - \cos(\lambda_{s,0})] \\ c_{\epsilon/2}^2 [\sin(\lambda_s(t) - \Omega) - \sin(\lambda_{s,0} - \Omega)] + s_{\epsilon/2}^2 [\sin(\lambda_s(t) + \Omega) - \sin(\lambda_{s,0} + \Omega)] \end{pmatrix} \quad (25)$$

If we neglect the smaller terms proportional to $s_{\epsilon/2}^2$ and we introduce the further hypothesis of equatorial orbit, Eq. 25 can be further simplified as

$$\begin{pmatrix} \delta e_x(t) \\ \delta e_y(t) \end{pmatrix} = R \begin{pmatrix} \cos(n_s t + \Phi_0) - \cos(\Phi_0) \\ \sin(n_s t + \Phi_0) - \sin(\Phi_0) \end{pmatrix} + \begin{pmatrix} \delta e_{x,0} \\ \delta e_{y,0} \end{pmatrix} \quad (26)$$

where

$$R = \frac{3 F_{srp} c_{\epsilon/2}^2}{2 \sqrt{\mu} n_s} \sqrt{a} \Delta B \quad \Phi_0 = \lambda_{s,0} - \Omega \quad (27)$$

The relative eccentricity vector circulates in one year of 360° starting from its initial condition as depicted in Fig. 1. The circulation size (R) is proportional to the square-root of the chief orbit semi-major axis and to the ballistic coefficient difference. The circulation center position (Φ_0) is related to the angle between the Sun ecliptic longitude at initial time and the chief Ω (approximated as constant). The exact circular shape is lost when including terms in inclination (Eq. 25) and higher-order terms in eccentricity (Appendix B), but, as will be shown in the following of the paper, the propriety of running close elliptical paths in one year remains. A similar motion of the *absolute* eccentricity vector in its phase space was previously analyzed in literature by Chao.³⁴

Sun and Moon Third-body Reduced Model

As done in the previous paragraph, it is of interest to isolate the most significant terms in the third-body plant matrix presented in Appendix B. First of all, the third-body out-plane effect is generally predominant

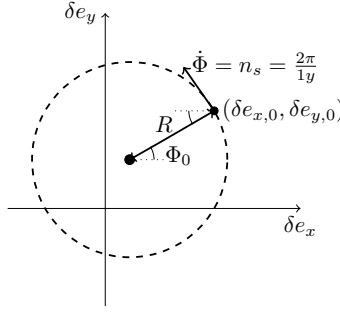


Figure 1: Relative eccentricity vector yearly circulation in near-circular equatorial orbit due to SRP (eclipses neglected).

with respect to the in-plane one. Therefore, the third-body action on the relative inclination vector components can be isolated. It is relevant to remember that third-body affects also ω and e , which induces effects on the relative eccentricity vector. Nevertheless, these effects are less significant than the ones on the relative inclination vector as will be highlighted by comparison with the numerical propagator. In order to simplify the formulation, the analysis can be restricted to the near-circular case by neglecting all the terms proportional to e^2 . Moreover, the third-body plant matrix comprises periodic oscillations related to the third-body fast variable u_3 , the formulations can be further greatly simplified by averaging over u_3 as $\frac{1}{2\pi} \int_0^{2\pi} \cdot du_3$. The doubly-averaged rates of variation of the relative inclination vector components in near-circular orbit, extracted from the third-body plant matrix, are

$$\begin{pmatrix} \dot{\delta i}_x \\ \dot{\delta i}_y \end{pmatrix} = \frac{3}{8} \sum_{j=1}^2 \frac{\mu_j}{r_j^3 n} \begin{bmatrix} -s_i s_{2i_j} \sin(\Omega - \Omega_j) + c_i s_{i_j}^2 \sin(2(\Omega - \Omega_j)) & \frac{c_i}{s_i} s_{2i_j} \cos(\Omega - \Omega_j) + 2s_{i_j}^2 \cos(2(\Omega - \Omega_j)) \\ -s_i^2(1 - 3c_{i_j}^2) - \frac{c_i(1+2s_i^2)}{s_i} s_{2i_j} \cos(\Omega - \Omega_j) - s_i^2 s_{i_j}^2 \cos(2(\Omega - \Omega_j)) & s_i s_{2i_j} \sin(\Omega - \Omega_j) - c_i s_{i_j}^2 \sin(2(\Omega - \Omega_j)) \end{bmatrix} \begin{pmatrix} \delta i_x \\ \delta i_y \end{pmatrix} \quad (28)$$

The summation is performed over the Sun and the Moon, μ_j is the third-body standard gravitational parameter, r_j is the third-body distance from the Earth center, n is the chief satellite mean motion, $\sin(\cdot) = s$ and $\cos(\cdot) = c$. In case of near-equatorial chief orbit, Eq. 28 can be further simplified by neglecting the terms proportional to s_i^2 on the bottom-left. The system of first-order differential equations expressed by Eq. 28 is time-variant. This is related to the third-body action on the chief i and Ω , and to the slight variation in time of the third-body ephemerides i_j and Ω_j , the Moon node line in particular precess in time. The two angles $\Omega - \Omega_j$ therefore vary in time and they can both assume the values 0° or 180° . In this case, for near-equatorial chief orbit, Eq.28 simplifies to

$$\begin{pmatrix} \dot{\delta i}_x \\ \dot{\delta i}_y \end{pmatrix} = \frac{3}{8} \sum_{j=1}^2 \frac{\mu_j}{r_j^3 n} \begin{bmatrix} 0 & \pm \frac{c_i}{s_i} s_{2i_j} + 2s_{i_j}^2 \\ \mp \frac{c_i}{s_i} s_{2i_j} & 0 \end{bmatrix} \begin{pmatrix} \delta i_x \\ \delta i_y \end{pmatrix} \quad (29)$$

Where the up and bottom signs are referred to the case of $\Omega - \Omega_j = 0^\circ$ and $\Omega - \Omega_j = 180^\circ$ correspondingly, which relate to either a parallel or anti-parallel alignment of the chief and third-bodies node lines, and derive from the cosines terms in Eq. 28. In Eq.29, the alignment of the apparent Sun, Moon and chief satellite orbit node lines is considered simultaneous in order to keep in the model the full lunisolar effect. Nevertheless, Eq.29 can be specified for the Sun and the Moon separately in case in which the two alignments take place at different times. The analytical procedure presented in the following is valid in both cases. The model in Eq.29 is still time-variant in i and i_j . Nevertheless, considering average values of i and i_j over the propagation time, the equations of δi_x and δi_y can be decoupled by derivating in time and substituting in one another. The resulting two second-order differential equations are

$$\begin{aligned} \ddot{\delta i}_x - \frac{9}{64} \sum_{j=1}^2 \left[\frac{\mu_j}{r_j^3 n} (\pm \frac{c_i}{s_i} s_{2i_j} + 2s_{i_j}^2) \right] \sum_{j=1}^2 \left[\frac{\mu_j}{r_j^3 n} (\mp \frac{c_i}{s_i} s_{2i_j}) \right] \delta i_x &= \ddot{\delta i}_x + \dot{\Theta}^2 \delta i_x = 0 \\ \ddot{\delta i}_y - \frac{9}{64} \sum_{j=1}^2 \left[\frac{\mu_j}{r_j^3 n} (\mp \frac{c_i}{s_i} s_{2i_j}) \right] \sum_{j=1}^2 \left[\frac{\mu_j}{r_j^3 n} (\pm \frac{c_i}{s_i} s_{2i_j} + 2s_{i_j}^2) \right] \delta i_y &= \ddot{\delta i}_y + \dot{\Theta}^2 \delta i_y = 0 \end{aligned} \quad (30)$$

For the Sun and the Moon, the terms containing $s_{i_j}^2$ are smaller than the terms containing s_{2i_j} , which in addition are amplified by $\frac{c_i}{s_i}$, significant in the near-equatorial case. Therefore, $\dot{\Theta}^2$ is positive and the two equations represent two harmonic oscillators. The initial conditions are: $\delta i_{x,0}$, $\delta i_{y,0}$, $(\delta \dot{i}_{x,0})$ and $(\delta \dot{i}_{y,0})$. The initial conditions on the first-order time derivatives can be linked to $\delta i_{x,0}$ and $\delta i_{y,0}$ through Eq. 29. Integrating results in

$$\begin{pmatrix} \delta i_x(t) \\ \delta i_y(t) \end{pmatrix} = \begin{bmatrix} \cos(\dot{\Theta}t) & \frac{\frac{3}{8} \sum_{j=1}^2 \frac{\mu_j}{r_j^3 n} (\pm \frac{c_i}{s_i} s_{2i_j} + 2s_{i_j}^2)}{\dot{\Theta}} \sin(\dot{\Theta}t) \\ \frac{\frac{3}{8} \sum_{j=1}^2 \frac{\mu_j}{r_j^3 n} (\mp \frac{c_i}{s_i} s_{2i_j})}{\dot{\Theta}} \sin(\dot{\Theta}t) & \cos(\dot{\Theta}t) \end{bmatrix} \begin{pmatrix} \delta i_{x,0} \\ \delta i_{y,0} \end{pmatrix} \quad (31)$$

with

$$\dot{\Theta} = \frac{3}{8} \sqrt{\sum_{j=1}^2 [\frac{\mu_j}{r_j^3 n} (\pm \frac{c_i}{s_i} s_{2i_j} + 2s_{i_j}^2)] \sum_{j=1}^2 [\frac{\mu_j}{r_j^3 n} (\pm \frac{c_i}{s_i} s_{2i_j})]} \quad (32)$$

Neglecting the smaller terms containing $s_{i_j}^2$, the model further simplifies to

$$\begin{pmatrix} \delta i_x(t) \\ \delta i_y(t) \end{pmatrix} = \begin{bmatrix} \cos(\dot{\Theta}t) & \pm \sin(\dot{\Theta}t) \\ \mp \sin(\dot{\Theta}t) & \cos(\dot{\Theta}t) \end{bmatrix} \begin{pmatrix} \delta i_{x,0} \\ \delta i_{y,0} \end{pmatrix} \quad (33)$$

with

$$\dot{\Theta} = \dot{\Theta}_{Sun} + \dot{\Theta}_{Moon} = \frac{3}{8} \sum_{j=1}^2 \frac{\mu_j}{r_j^3 n} \frac{c_i}{s_i} s_{2i_j} = \frac{3}{8} \frac{\mu_{Sun}}{r_{Sun}^3 n} \frac{c_i}{s_i} s_{2i_{Sun}} + \frac{3}{8} \frac{\mu_{Moon}}{r_{Moon}^3 n} \frac{c_i}{s_i} s_{2i_{Moon}} \quad (34)$$

which represents a rotation of the relative inclination vector, either clockwise in the $\Omega - \Omega_j = 0^\circ$ case or counterclockwise in the $\Omega - \Omega_j = 180^\circ$ case, as depicted in Fig. 2. The rotation rate depends on the chief orbit inclination (which is assumed small for the near-equatorial assumption), chief orbit size, third-body orbit inclination, mass and distance from the Earth. Moreover, under the hypothesis of simultaneous alignment of the two third-bodies and chief orbit node lines, the rate is a superposition of a component due to the Sun and a component due to the Moon. In case of not simultaneous alignment, the rotation of the relative inclination vector due to the Sun and the rotation due to the Moon don't superimpose instantaneously but take place at different times. A similar motion of the *absolute* inclination vector in its phase space for a GEO was previously analyzed in literature by Chao.³⁴ Differently from the absolute case, the presented relative motion model identifies the presence of either a clockwise or counterclockwise rotation of the relative inclination vector, in correspondence of either a parallel or anti-parallel alignment of the chief and third-body orbit node line.

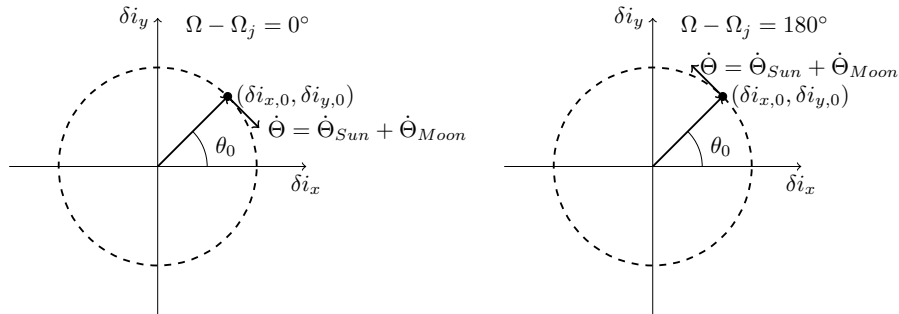


Figure 2: Relative inclination vector rotation in near-circular near-equatorial orbit due to Sun and Moon third-body effect.

VALIDATION AND PERFORMANCE ASSESSMENT

The validation reference numerically integrates the equations of motion with perturbations for both the chief and deputy satellites. Tab. 3 describes the numerical solver and the assumptions made for expressing the perturbing accelerations. The ground-truth identified by the numerical propagator replicates the main

Table 3: Numerical solver.

Integrator	Explicit Runge-Kutta (4,5) (Dormand-Prince). Variable step = [5, 15]s or [30, 60]s
SRP	Constant satellite cross-section normal to the Sun, no eclipses.
Third-body	Lunar and solar point masses, analytical ephemerides.
Geopotential	J_2 and/or J_3 .

hypotheses taken to formalize the analytical models, e.g., no eclipses for SRP, no atmospheric drag and only J_2/J_3 components for the geopotential. This permits to isolate the errors intrinsic to the linear analytical modeling with respect to the numerical integration, without mixing with the further inevitable errors associated to perturbative components that are not modeled in this paper (e.g. eclipses effects, differential drag or higher-order geopotential terms). Moreover, the selection of this truncated force model permits to test and validate each plant matrix also in orbital regimes in which the modeled perturbation is not the only or most significant one. The errors associated to the effects not included in the ground-truth have been evaluated a posteriori as presented in the next paragraph. According to these considerations, the validation has been performed in three steps. Firstly, each single plant matrix (plus the Keplerian motion) has been validated with respect to the numerical integrator which includes only the disturbing acceleration correspondent to the modeled perturbation. Secondly, the complete plant matrix (Eq. 15) has been validated and its performances assessed with respect to the numerical reference that now includes all the disturbing accelerations presented in Tab. 3. Thirdly, the accuracy provided by the two reduced models is assessed by comparison with respect to both the numerical integrator and the full analytical models. In Tab. 3, the two integration step windows considered are used in relation to the size of the reference chief orbit analyzed. A chief satellite with mass of 100kg, constant SRP reference illuminated area of 1m^2 and reflectivity coefficient of 1.88 is considered. ΔB_{srp} is hypothesized constant equal to 2% of B_{srp} .

The described validation procedure has been performed for satellites formations in different orbital regimes,

Table 4: Chief absolute motion (top) and relative motion (bottom) osculating initial conditions.

	LEO	GPS	GEO	HEO
Epoch date	1 January 2016	1 January 2016	1 January 2016	1 January 2016
Epoch time (hh.mm.ss)	00.00.00	00.00.00	00.00.00	00.00.00
h_p	514.88km	20129km	35766km	353km
e	0.001	0.0019	0.0005	0.7459
i	97.44°	55.341°	3°	30°
Ω	0°	0°	280°	0°
ω	45°	45°	45°	45°
M	0°	0°	0°	0°

$a\delta i$	$2a\delta e$	θ	φ	$a\delta a$	$a\delta \lambda$
3.5km	0.25km	45°	45°	0km	0km

both circular (LEO, the Global Positioning System medium Earth orbit - GPS, GEO) and highly elliptical orbit (HEO). The initial osculating chief orbital elements and initial osculating ROE are reported in Tab. 4. These initial conditions guarantee full coupling of all ROE variations. From the chief and ROE osculating

initial conditions, the deputy osculating initial conditions can be obtained. An analytical osculating to mean space transformation under the variety of perturbation considered does not exist in literature. Therefore, numerical averaging over each chief satellite period has been applied. An initialization interval of some orbits is necessary to obtain averaged mean chief and deputy initial conditions from which the mean initial ROE state is computed and then propagated analytically. Regarding the numerical integrator, its Cartesian outputs have been converted to osculating chief and deputy orbital elements and then averaged prior mean ROE state computation. It is relevant to remember that $\delta a_{osc.} = 0$ doesn't imply a null mean initial condition δa . A linear drift in along-track direction is therefore expected. This does not constitute a problem thanks to the presented models validity for arbitrary large values of $\delta\lambda$, moreover, it permits to validate also the first plant matrices column. The propagation horizons considered are 10 and 100 orbits to evaluate the medium and long-term accuracy, and 1 year to capture the yearly lunisolar effects.

The metric considered for validation purposes is the absolute error with respect to the reference and the maximum value it assumes over the propagation time span

$$\epsilon_{\delta\chi_j}(t) = |a\delta\chi_{j,mean}(t)^{STM} - a\delta\chi_{j,mean}(t)^{num.}|, \quad \epsilon_{\delta\chi_j} = \max_i \epsilon_{\delta\chi_j}(t_i) \quad j = 1, \dots, 6 \quad (35)$$

Moreover, it is useful to have a direct insight on the weight of the maximum error with respect to the ROE variation in the propagation interval. In this sense, the number of accurate digits with which the analytical propagator is able to provide, in the worst case, the ROE maximum absolute variations is computed as

$$n_{a.d.,\delta\chi_j} = \mathcal{O}(\Delta_{\delta\chi_j}) - \mathcal{O}(\epsilon_{\delta\chi_j}) \quad j = 1, \dots, 6 \quad (36)$$

where

$$\Delta_{\delta\chi_j} = \max_i (|a\delta\chi_{j,mean}(t_i)^{num.} - a\delta\chi_{j,mean}(t_0)^{num.}|) \quad j = 1, \dots, 6 \quad (37)$$

Plant matrices validation results and performance

In the following, Tab. 5 to Tab. 7 report the validation results of SRP, Sun and Moon third-body, J_2 and J_3 plant matrices (summed to Keplerian motion). Tab. 8 instead validates the complete plant matrix in Eq. 15. Looking at Tab. 5, the effect of SRP on the relative eccentricity vector components increases with the size of the orbit. In both GPS orbit, GEO and HEO, variations of the order of a hundred meters or more are reached in one year. The SRP plant matrix models δe_x and δe_y with a level of accuracy of at least one digit. The worst case is the error committed on the x-component in one year in GEO ($\epsilon_{\delta e_x} = 13.8\text{m}$), which anyway is lower than 4% of its maximum variation ($\Delta_{\delta e_x} = 350\text{m}$). The effect of SRP on the relative inclination vector components is considerably less significant, almost always under the meter level. Nevertheless, the accuracy provided by the SRP plant matrix on δi_x and δi_y is usually of at least one digit, as it is for $\delta\lambda$. Looking at Tab. 6, the third-body effect increases by increasing the orbit size. Variations of the relative inclination vector components up to one hundred meters are reached in one year in GEO, and up to 54.5m in HEO. The third-body plant matrix models δi_x and δi_y with a level of accuracy usually of at least one digit on 100 orbits and one year. The worst case is the error committed on the y-component in one year in GEO ($\epsilon_{\delta i_y} = 6.98\text{m}$), which anyway is lower than 7% of its maximum variation ($\Delta_{\delta i_y} = 103\text{m}$). The effect of third-body on the relative eccentricity vector components is smaller, up to 13.5m in one year in GEO and up to 26m in HEO. The accuracy provided by the third-body plant matrix on δe_x and δe_y is affected by the not inclusion of the long-periodic terms in the equations of e and ω reported in Appendix A. The maximum not-modeled long-periodic effect arrives at 25.7m in one year in HEO. Nevertheless, the inclusion in the model of the secular drift of ω permits to follow the secular behavior of the relative eccentricity vector components. $\delta\lambda$ is in great part not-modeled by the third-body plant matrix, which is affected by the absence of an expression for the third-body effect on the fast variable in the model in Appendix A.

Looking at Tab. 7, the effects of J_2 on the relative eccentricity and inclination vectors are expected and extensively described in literature.²⁰ J_3 affects both the two relative vectors, but considerably less significantly than J_2 (effects under 2m). The propagation accuracy provided by the J_2 and J_3 plant matrices on both the relative vectors components and $\delta\lambda$ is of at least one digit.

δa is not significantly affected by the considered perturbations and its variation is not modeled by the plant matrices.

Table 5: SRP plant matrix validation with respect to the numerical reference, for relative motion perturbed by only solar radiation pressure (without eclipses).

	time	$a\delta a$		$a\delta\lambda$		$a\delta e_x$		$a\delta e_y$		$a\delta i_x$		$a\delta i_y$	
		$\epsilon_{\delta a}$ (m)	$\Delta_{\delta a}$ (m)	$\epsilon_{\delta\lambda}$ (m)	$\Delta_{\delta\lambda}$ (m)	$\epsilon_{\delta e_x}$ (m)	$\Delta_{\delta e_x}$ (m)	$\epsilon_{\delta e_y}$ (m)	$\Delta_{\delta e_y}$ (m)	$\epsilon_{\delta i_x}$ (m)	$\Delta_{\delta i_x}$ (m)	$\epsilon_{\delta i_y}$ (m)	$\Delta_{\delta i_y}$ (m)
LEO	10 o.	10^{-6}	10^{-7}	10^{-5}	0.02	10^{-5}	0.03	10^{-4}	0.02	10^{-6}	10^{-4}	10^{-6}	10^{-4}
	100 o.	10^{-6}	10^{-6}	10^{-3}	0.24	10^{-4}	0.34	10^{-3}	0.27	10^{-6}	10^{-3}	10^{-5}	10^{-3}
	1 y.	10^{-5}	10^{-5}	1.40	11.3	0.10	3.58	0.62	23.1	0.04	0.04	0.04	0.04
GPS	10 o.	10^{-5}	10^{-5}	0.01	6.92	0.02	5.78	0.12	1.43	10^{-4}	10^{-3}	10^{-4}	10^{-3}
	100 o.	10^{-4}	10^{-4}	0.10	77.6	0.10	52.1	1.99	43.5	10^{-3}	0.05	10^{-3}	0.06
	1 y.	10^{-4}	10^{-4}	0.12	563	2.82	86.8	5.24	174	0.01	0.08	0.02	0.12
GEO	10 o.	10^{-4}	10^{-5}	0.04	35.7	0.96	1.29	0.03	25.8	10^{-3}	10^{-3}	10^{-4}	10^{-4}
	100 o.	10^{-4}	10^{-4}	0.20	392	13.2	198	2.14	170	0.02	0.01	0.01	0.03
	1 y.	10^{-3}	10^{-3}	3.08	10^3	13.8	350	7.74	170	0.05	0.03	0.01	0.03
HEO	10 o.	10^{-5}	10^{-5}	0.19	16.0	0.02	5.08	0.08	0.34	10^{-4}	0.65	10^{-4}	0.65
	100 o.	10^{-4}	10^{-4}	4.13	144	0.12	46.3	1.28	22.9	0.04	6.18	0.04	6.18
	1 y.	0.04	0.04	156	10^3	2.5	75.1	3.5	116	0.34	8.86	0.35	8.87

Table 6: Third-body plant matrix validation with respect to the numerical reference for relative motion perturbed by only Sun and Moon third-body effect.

	time	$a\delta a$		$a\delta\lambda$		$a\delta e_x$		$a\delta e_y$		$a\delta i_x$		$a\delta i_y$	
		$\epsilon_{\delta a}$ (m)	$\Delta_{\delta a}$ (m)	$\epsilon_{\delta\lambda}$ (m)	$\Delta_{\delta\lambda}$ (m)	$\epsilon_{\delta e_x}$ (m)	$\Delta_{\delta e_x}$ (m)	$\epsilon_{\delta e_y}$ (m)	$\Delta_{\delta e_y}$ (m)	$\epsilon_{\delta i_x}$ (m)	$\Delta_{\delta i_x}$ (m)	$\epsilon_{\delta i_y}$ (m)	$\Delta_{\delta i_y}$ (m)
LEO	10 o.	10^{-6}	10^{-7}	0.01	0.02	10^{-3}	10^{-3}	10^{-3}	10^{-3}	10^{-4}	0.01	10^{-4}	0.01
	100 o.	10^{-6}	10^{-6}	0.02	0.13	0.01	0.01	0.01	0.01	10^{-3}	0.04	10^{-3}	0.12
	1 y.	10^{-4}	10^{-4}	13.0	17.8	0.10	0.11	1.30	1.30	0.50	1.42	0.50	6.31
GPS	10 o.	10^{-5}	10^{-5}	0.64	1.19	0.02	0.03	0.08	0.09	0.22	0.01	0.06	0.11
	100 o.	10^{-4}	10^{-4}	17.9	21.7	0.38	0.31	0.14	0.21	0.44	2.42	0.12	1.42
	1 y.	10^{-4}	10^{-4}	94.8	129	1.26	0.84	2.78	3.29	0.44	18.8	0.27	2.18
GEO	10 o.	10^{-4}	10^{-4}	5.12	5.76	2.33	2.13	1.22	0.84	2.88	5.74	2.39	3.80
	100 o.	10^{-3}	10^{-3}	27.4	41.28	5.05	5.19	3.17	3.10	4.16	24.8	4.38	23.7
	1 y.	10^{-3}	10^{-3}	132	171	5.64	5.19	9.27	13.5	6.79	86.6	6.98	103
HEO	10 o.	10^{-3}	10^{-3}	1.28	3.45	1.71	2.08	1.63	1.24	0.40	0.09	0.26	0.36
	100 o.	0.02	0.02	18.7	21.0	13.7	20.0	6.05	9.59	1.66	6.70	1.66	13.5
	1 y.	1.30	1.30	10^3	10^3	22.6	23.5	20.3	25.7	2.59	11.0	2.73	54.5

Table 7: J_2 (top) and J_3 (bottom) plant matrices validation with respect to the numerical reference for relative motion perturbed by only J_2 (top) or J_3 (bottom).

	time	$a\delta a$		$a\delta\lambda$		$a\delta e_x$		$a\delta e_y$		$a\delta i_x$		$a\delta i_y$	
		$\epsilon_{\delta a}$ (m)	$\Delta_{\delta a}$ (m)	$\epsilon_{\delta\lambda}$ (m)	$\Delta_{\delta\lambda}$ (m)	$\epsilon_{\delta e_x}$ (m)	$\Delta_{\delta e_x}$ (m)	$\epsilon_{\delta e_y}$ (m)	$\Delta_{\delta e_y}$ (m)	$\epsilon_{\delta i_x}$ (m)	$\Delta_{\delta i_x}$ (m)	$\epsilon_{\delta i_y}$ (m)	$\Delta_{\delta i_y}$ (m)
LEO	10 o.	10^{-3}	10^{-4}	0.21	86.0	0.21	3.22	0.59	3.07	10^{-4}	10^{-4}	0.02	191
	100 o.	10^{-3}	10^{-3}	2.53	945	0.57	27.9	6.00	38.5	10^{-3}	10^{-3}	0.58	10^3
GPS	10 o.	10^{-4}	10^{-4}	10^{-3}	25.3	10^{-5}	0.10	10^{-4}	0.10	10^{-5}	10^{-5}	10^{-3}	8.87
	100 o.	10^{-4}	10^{-4}	0.05	281	10^{-4}	1.16	10^{-3}	1.14	10^{-5}	10^{-5}	0.03	98.5
GEO	10 o.	10^{-6}	10^{-6}	10^{-3}	0.32	10^{-4}	0.37	10^{-4}	0.36	10^{-5}	10^{-8}	10^{-5}	0.01
	100 o.	10^{-6}	10^{-6}	0.01	3.64	10^{-3}	4.30	10^{-4}	3.98	10^{-5}	10^{-5}	10^{-4}	0.16
HEO	10 o.	0.14	0.13	34.7	10^4	0.20	54.1	0.19	51.4	0.01	0.01	0.01	4.3
	100 o.	1.57	1.57	389	10^5	2.90	778	4.77	302	0.1	0.1	2.0	48.0

	time	$a\delta a$		$a\delta\lambda$		$a\delta e_x$		$a\delta e_y$		$a\delta i_x$		$a\delta i_y$	
		$\epsilon_{\delta a}$ (m)	$\Delta_{\delta a}$ (m)	$\epsilon_{\delta\lambda}$ (m)	$\Delta_{\delta\lambda}$ (m)	$\epsilon_{\delta e_x}$ (m)	$\Delta_{\delta e_x}$ (m)	$\epsilon_{\delta e_y}$ (m)	$\Delta_{\delta e_y}$ (m)	$\epsilon_{\delta i_x}$ (m)	$\Delta_{\delta i_x}$ (m)	$\epsilon_{\delta i_y}$ (m)	$\Delta_{\delta i_y}$ (m)
LEO	10 o.	10^{-6}	10^{-7}	0.02	0.01	10^{-4}	0.15	10^{-6}	10^{-5}	10^{-6}	10^{-4}	10^{-5}	10^{-3}
	100 o.	10^{-6}	10^{-6}	0.28	0.16	10^{-3}	1.60	10^{-6}	10^{-4}	10^{-6}	10^{-3}	10^{-5}	0.08
HEO	10 o.	10^{-5}	10^{-5}	0.28	5.99	10^{-5}	0.16	10^{-5}	0.15	10^{-6}	0.04	0.05	0.08
	100 o.	10^{-5}	10^{-5}	3.05	66.5	10^{-4}	1.77	10^{-4}	1.70	10^{-5}	0.47	0.51	0.93

Table 8: STM (Eq. 22) validation with respect to the numerical reference for relative motion perturbed by SRP, Sun and Moon third-body, J_2 and J_3 . The corresponding plots are reported in Appendix C.

	time	$a\delta a$		$a\delta \lambda$		$a\delta e_x$		$a\delta e_y$		$a\delta i_x$		$a\delta i_y$	
		$\epsilon_{\delta a}$ (m)	$\Delta_{\delta a}$ (m)	$\epsilon_{\delta \lambda}$ (m)	$\Delta_{\delta \lambda}$ (m)	$\epsilon_{\delta e_x}$ (m)	$\Delta_{\delta e_x}$ (m)	$\epsilon_{\delta e_y}$ (m)	$\Delta_{\delta e_y}$ (m)	$\epsilon_{\delta i_x}$ (m)	$\Delta_{\delta i_x}$ (m)	$\epsilon_{\delta i_y}$ (m)	$\Delta_{\delta i_y}$ (m)
LEO	10 o.	10^{-3}	10^{-3}	0.43	85.2	0.06	2.94	0.14	2.81	10^{-3}	0.01	0.02	190
	100 o.	0.01	0.01	3.11	937	1.11	26.7	1.51	36.1	0.01	0.06	0.06	10^3
	1 y.	0.8	0.8	112	10^4	40.9	357	20.2	400	1.76	91	9.89	10^5
GPS	10 o.	10^{-4}	10^{-6}	0.63	17.1	0.04	5.64	0.20	1.64	0.22	0.01	0.07	8.99
	100 o.	10^{-4}	10^{-4}	17.8	182	0.50	50.0	2.08	45.6	0.44	2.62	0.12	97.1
	1 y.	10^{-3}	10^{-3}	93.4	10^3	4.11	100	7.18	176	0.46	20.9	0.48	724
GEO	10 o.	10^{-3}	10^{-4}	5.19	41.7	2.02	2.61	0.66	26.6	2.89	5.69	2.39	3.74
	100 o.	10^{-3}	10^{-3}	26.4	439	22.2	219	5.73	168	4.36	26.2	4.48	24.7
	1 y.	0.01	0.01	121	10^3	42.2	377	18.6	183	7.11	53.2	7.17	66.1
HEO	10 o.	0.17	0.17	35.0	10^4	1.82	61.1	1.99	49.5	0.39	0.56	0.37	4.47
	100 o.	1.68	1.68	375	10^5	16.4	731	8.61	246	1.53	2.88	2.78	18.4
	1 y.	19.6	19.6	10^3	10^5	138	10^3	44.9	10^3	6.83	30.0	25.9	144

Table 9: CPU time for the STM and numerical propagations of the relative motion perturbed by SRP, Sun and Moon third-body, J_2 and J_3 .

		LEO			GPS			GEO			HEO		
		10 o.	100 o.	1 y.	10 o.	100 o.	1 y.	10 o.	100 o.	1 y.	10 o.	100 o.	1 y.
CPU time	STM (s)	0.39	0.46	5.97	0.34	0.48	0.91	0.34	0.47	0.71	0.34	0.48	0.99
	Num. (s)	9.41	46.0	646	21.2	322	572	44.0	169	622	23.0	339	1787

The final accuracy budget is obtained looking at Tab. 8. Summarizing, in LEO and GPS orbit, effects bigger than 1m are modeled with at least one accurate digit and a maximum of five. In GEO and HEO, effects bigger than 10m are modeled with at least one accurate digit and a maximum of two. The behavior in time of the absolute error, $\epsilon_{\delta \chi_j}(t)$ is shown by the plots in Appendix C. The error is usually not linear but oscillates in time with repeated patterns. This error can be attributed mainly to the approximations inherited from the hypotheses underlying the models in Appendix A, and to the terms truncated by the first-order Taylor expansion. In terms of propagation time, this error behavior implies that the analytical propagator provides fairly accurate results on the medium/long-term, modeling so the long-periodic and secular ROE variation under the considered perturbations. In particular, at least one accurate digit is guaranteed in LEO on propagation equal or longer than 10 orbits and in GPS orbit, GEO and HEO on propagation equal or longer than 100 orbits (except δi_x in HEO). To complete the analysis, the errors associated to the effects not included in the ground-truth have to be evaluated. The error related to the not-modeled eclipses can be obviated by means of the introduction of a simple shadow function.³⁵ The error associated to the not-modeled differential drag can be obviated by combining the STM formalized in this paper with the one of Koenig et al.,²⁶ incrementing the relative state by the relative semi-major axis and eccentricity vector components time variations. The error related to the not-modeled higher-order geopotential components instead has to be added. Reliable evaluation of this error can be found in literature. Mahajan et al.¹⁹ evaluate the error on the relative position of a formation in LEO as a function of the degree of the zonal harmonics modeled. The considered ground-truth includes a 70×0 gravity model. The error introduced by neglecting harmonics with degree higher than three is comprised in between 7m and 13m in ten days of propagation, depending on the LEO inclination. By increasing the orbit size, this error will inevitably drop together with the geopotential effect on the orbital motion. A final remark has to be done regarding the truncation error introduced by the numerical integrator on a long-term propagation. To evaluate the accuracy of the numerical solver selected, it has been compared with a different integration technique (the Adams-Bashforth-Moulton multistep method). On one year of propagation, the maximum differences between the two numerical propagators outputs are at least one order

of magnitude lower than the level of accuracy provided by the analytical propagator. Therefore, the selection of a different numerical integrator does not impact the results just presented. Finally, the performances in terms of computational efficiency (i.e., Central Processing Unit, CPU, time) are assessed in Tab. 9. The STM outperforms the numerical integrator in terms of computational efficiency, being at least 24 times, 100 times and 108 times faster in case of 10 orbits, 100 orbits and 1 year of propagation correspondingly.

Reduced models validation results and performance

The assumption that SRP mainly affects the relative eccentricity vector and the Sun and Moon third-body mainly affects the relative inclination vector has to be validated. Tab. 10 extracts the effects bigger than 10m in 100 orbits from Tab. 5 to Tab. 7. Evidently, the assumption made is fairly accurate, with the exception of the HEO in which Sun and Moon third-body causes significant effects also on the relative eccentricity vector.

Table 10: Perturbation effects budget. Effects bigger than 10m in 100 orbits are considered.

	δe_x	δe_y	δi_x	δi_y
LEO	J ₂	J ₂		J ₂
GPS	SRP	SRP		J ₂
GEO	SRP	SRP	TB	TB
HEO	J ₂ ,SRP,TB	J ₂ ,SRP,TB		J ₂ ,TB

SRP reduced model validation Fig. 3 shows the relative eccentricity vector tip motion in its phase space in one year of propagation under the effect of SRP (neglecting eclipses). It considers formations in the LEO, GPS orbit, GEO and HEO analyzed previously varying the ballistic coefficient difference between the two spacecraft. The colored lines are obtained by analytical propagation (SRP plus Keplerian plant matrices), the black dotted lines by numerical integration. The relative eccentricity vector runs a close elliptical path

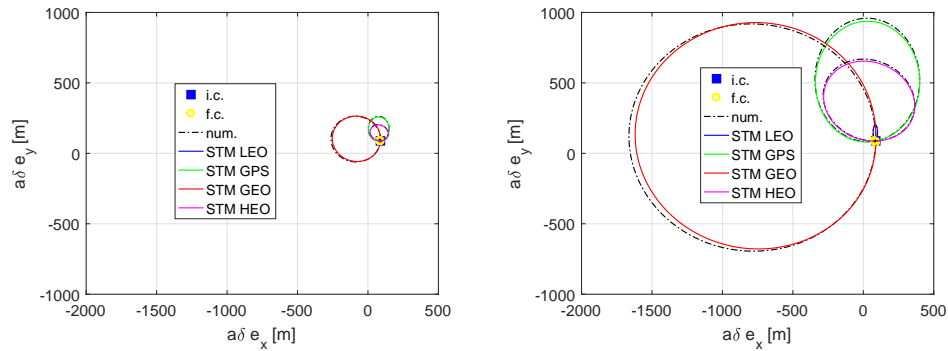


Figure 3: Relative eccentricity vector tip motion in its phase space due to SRP (eclipses neglected) in one year of propagation in LEO, GPS orbit, GEO and HEO. $\Delta B = 2\%$ (left), $\Delta B = 10\%$ (right). The initial phase angle is $\varphi = 45^\circ$.

in one year as it was predicted by the reduced analytical model. Moreover, as expected, the dimensions of this close path increase together with the size of the chief orbit (semi-major axis) and the ballistic coefficient difference. For formations not in LEO, these dimensions are significant, from hundred meters up to more than one kilometer in GEO with $\Delta B = 10\%$. In Fig. 4, the reduced SRP model is validated with respect to both numerical integration and the full analytical model in both near-circular, near-equatorial and eccentric orbits. The reduced model provides good results in the near-circular case. In particular, Eq. 26 is accurate in near-circular near-equatorial orbits (Fig. 4 top-left), whereas Eq. 25 is accurate in near-circular inclined orbits

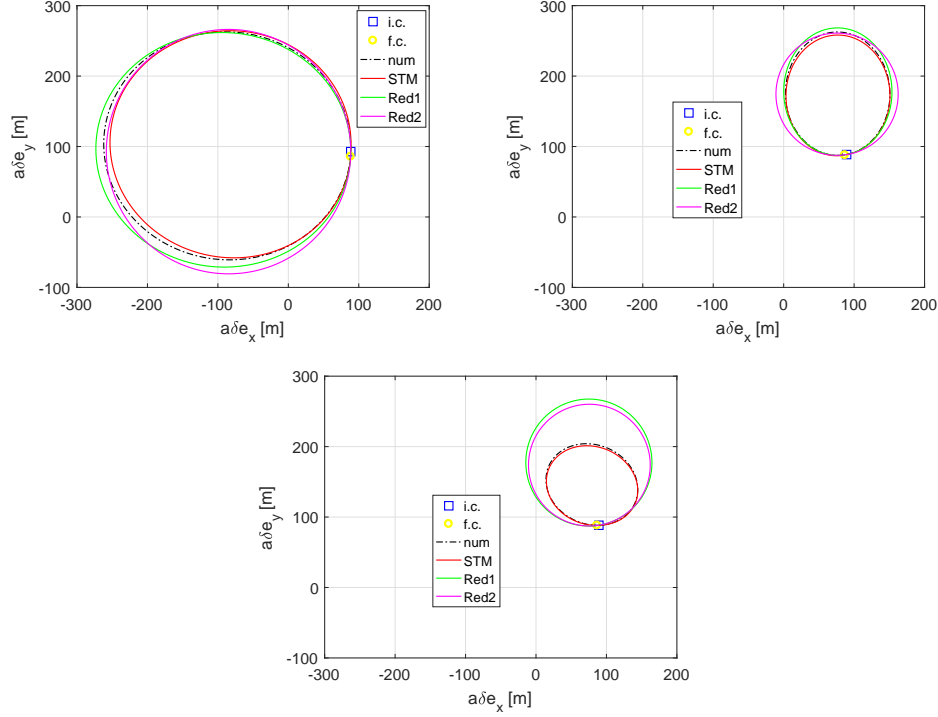


Figure 4: Reduced SRP models validation for GEO (top-left), GPS orbit (top-right) and HEO (bottom), with $\Delta B = 2\%$. "Red1" refers to Eq. 25, "Red2" refers to Eq. 26.

(Fig. 4 top-right). This is expected considering that Eq. 26 has been obtained for zero inclination. Both Eq. 26 and Eq. 25 fail in eccentric orbit (Fig. 4 bottom) since they neglect terms proportional to e^2 . The complete plant matrix provides instead accurate results in all the considered orbits. The values of the circulation radius and initial phase according to Eq. 27 are reported in Tab. 11. Both these values are accurate in GEO. The initial phase is fairly accurate also in GPS orbit and HEO, where instead the purely circular approximation doesn't hold anymore. Looking at Fig. 3, it can be noticed how the relative eccentricity vector either librates

Table 11: Radius and initial phase of the circulation path according to Eq. 27.

	GEO	GPS	HEO
$aR[m]$	173.50	86.74	86.34
$\Phi_0[^\circ]$	-360.01	-81.01	-81.01

(LEO, GPS orbit and HEO) or circulates (GEO) in its phase space. The transition is related to the dimensions and orientation of its close trajectory. Dimensions and orientation are themselves related to the chief orbit size, the ballistic coefficient difference, the inclination with respect to the ecliptic, the position of the Sun in the chief orbital plane and the initial condition of the relative motion (e.g. initial phase angle φ , Fig. 5). All these elements are present in Eq. 25.

A physical interpretation of the relative eccentricity vector motion can be suggested. SRP induces yearly-periodic oscillations of the eccentricity and argument of perigee of the chief and deputy orbits in dependence of the Sun position with respect to the orbits perigees.³⁴ These periodic behaviors of the absolute parameters translate in a yearly-periodic oscillation of the modulus and/or phase of the relative eccentricity vector which causes the close path trajectories. Further analysis of this physical interpretation is presented by the first author of this paper in his thesis.³⁶

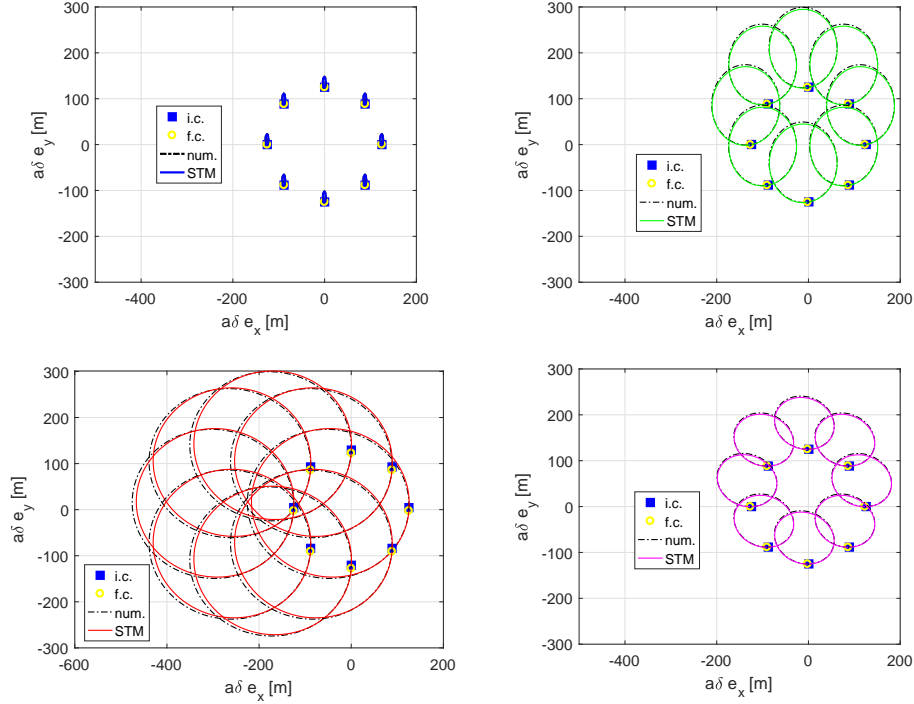


Figure 5: Relative eccentricity vector motion varying the initial phase angle. In LEO (top-left), GPS orbit (top-right), GEO (bottom-left) and HEO (bottom-right), with $\Delta B = 2\%$.

Sun and Moon third-body reduced model validation Fig. 6 shows the motion of the relative inclination vector tip in its phase space in 2400days of propagation under the action of Sun and Moon third-body. It considers formations in two GEOs, the first with $i = 3^\circ$ and $\Omega = 280^\circ$, the second with $i = 7.3^\circ$ and $\Omega = 353^\circ$ and in the HEO analyzed previously. The colored lines are the ones obtained through analytical propagation (third-body plus Keplerian plant matrices), the black dotted lines instead are obtained by numerical integration. The relative inclination vector of the two GEOs almost perfectly rotates around the origin of its phase

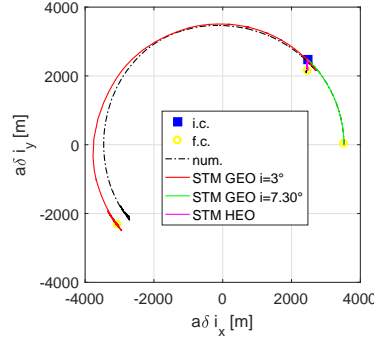


Figure 6: Relative inclination vector tip motion in its phase space due to Sun and Moon third-body in 2400days of propagation in GEO ($i = 3^\circ$, $\Omega = 280^\circ$), GEO ($i = 7.3^\circ$, $\Omega = 353^\circ$) and HEO. The initial phase angles is $\theta = 45^\circ$.

space, in either clockwise or counterclockwise direction, as it was predicted by the reduced analytical model. However, in the HEO case the movement is much less significant. In order to further validate the reduced model, the histories of variation in time of the angles $\Omega - \Omega_{Sun}$ and $\Omega - \Omega_{Moon}$ for the two GEOs are reported

in Fig. 7. For the less inclined GEO, these angles vary consistently and they both assume a value of 180°

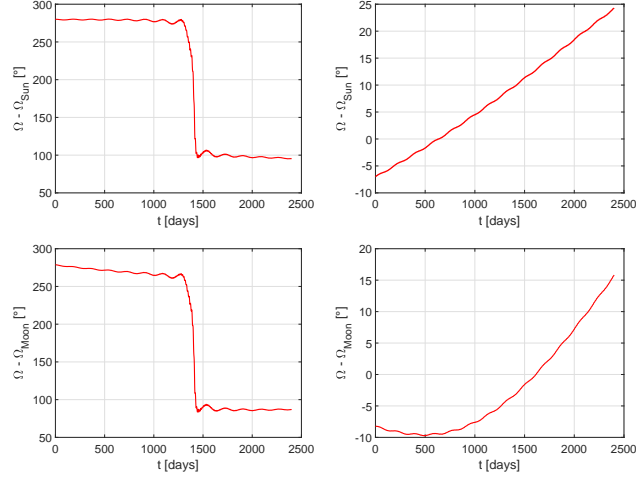


Figure 7: Chief satellite orbit node respect to ecliptic node (top) and respect to Moon orbit node (bottom) in 2400days of propagation in GEO with $i = 3^\circ$ and $\Omega = 280^\circ$ (left) and in GEO with $i = 7.3^\circ$ and $\Omega = 353^\circ$ (right).

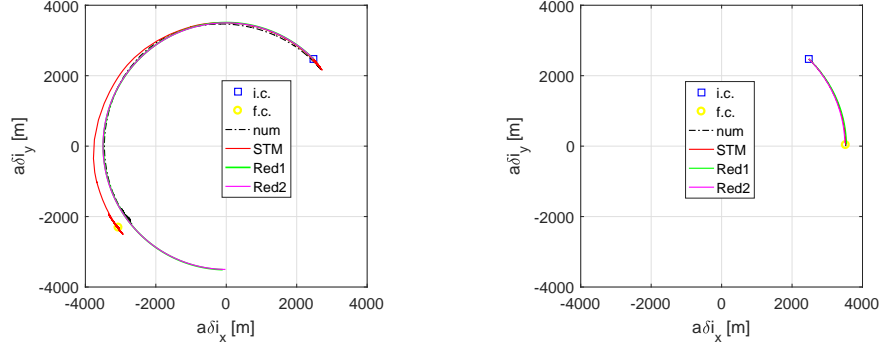


Figure 8: Reduced third-body models validation for GEO with $i = 3^\circ$ and $\Omega = 280^\circ$ (left) and GEO with $i = 7.3^\circ$ and $\Omega = 353^\circ$ (right). "Red1" refers to Eq. 31, whereas "Red2" refers to Eq. 33.

in correspondence of about half of the propagation time (Fig. 7 left). As anticipated by Eq. 33, this event corresponds to a counterclockwise rotation of the relative inclination vector. For the more inclined GEO, the two angles stay close to zero value for all the propagation (Fig. 7 right) and, as anticipated by Eq. 33, the relative inclination vector rotates clockwise. The reduced analytical model is therefore able to predict the physical behavior of the relative inclination vector in its phase space as a function of the relative orientation of the chief and third-bodies orbits node lines. In Fig. 8, the reduced third-body model is validated with respect to both numerical integration and the full analytical model. Mean values of i , i_{Sun} and i_{Moon} over the propagation time have been considered in the reduced models. The two models in Eq. 31 and Eq. 33 provide very similar results, therefore the inclusion of terms proportional to s_{ij}^2 doesn't impact significantly the model accuracy. Eq. 33 is accurate in GEO with $i = 7.3^\circ$, where both $\Omega - \Omega_{Sun}$ and $\Omega - \Omega_{Moon}$ stay close to zero for all the propagation time (Fig. 8 right). In case of GEO with $i = 3^\circ$ instead, the two angles reach the values of 180° only at half propagation. Therefore, applying Eq. 33 for all the propagation time leads to an overestimation of the path run by the vector (Fig. 8 left). This problem can be actually expected and solved by limiting the propagation to the interval in which $\Omega - \Omega_{Sun}$ and $\Omega - \Omega_{Moon}$ are close to 180° . Looking at the numerical reference trajectory, it can be observed how the majority of the vector motion is concentrated in occurrence of the anti-parallel alignment of the chief and third-bodies node lines, which happens approximately in between 1370 to 1430days. The reduced model actually almost matches the

exact final condition if used in this time interval. Close to the initial and final conditions, the node lines are not aligned and the vector motion is much less significant. Tab. 12 provides the rates of rotation according to Eq. 32 and Eq. 34, for the two GEOs considered. In case of GEO with $i = 3^\circ$, the presented rates

Table 12: Values of the relative inclination vector rotation rates. Subscript "1" refers to Eq. 32, subscript "2" refers to Eq. 34. The rates due to Sun and Moon in Eq. 34 are also reported.

	$\dot{\Theta}_1[^\circ/y]$	$\dot{\Theta}_2[^\circ/y]$	$\dot{\Theta}_{2,Sun}[^\circ/y]$	$\dot{\Theta}_{2,Moon}[^\circ/y]$
GEO $i = 3^\circ$	33.98	34.16	11.06	23.10
GEO $i = 7.3^\circ$	6.81	6.64	2.15	4.49

account for a rotation over 2400days. The rates for the second GEO are lower due to the greater inclination. The two reduced models provide again very similar results, but the second model permits to conclude on the weight that separately the Sun and the Moon have on the relative inclination vector rotation. In both GEOs, the Moon effect is always almost double than the one related to the Sun. This result is due to the fact that $\frac{\mu_{Moon}}{r_{Moon}^3}$ is greater than $\frac{\mu_{Sun}}{r_{Sun}^3}$, due to the lower distance of the Moon respect to the Earth that compensates the smaller mass. The inclinations of the apparent Sun and Moon orbits are instead very similar, the Moon orbit is inclined of about 5° with respect to the ecliptic.

A physical interpretation of the relative inclination vector motion can be suggested. The Sun and Moon attraction normal to the chief and deputy satellites orbital planes causes a torque about the lines of intersection of the satellites orbits and the apparent Sun and Moon orbits.¹³ When $\Omega - \Omega_{Sun}$ and $\Omega - \Omega_{Moon}$ are either 0° or 180° these lines of intersection stay on the equator. The gravitational torques that act about these two lines cause a gyroscopic effect that determines a regression of these lines on the apparent Sun and Moon orbital planes, which are instantaneously intersecting the equator. It causes a variation of the satellites RAAN with almost no effect on the inclination.³⁴ This behavior of the absolute parameters translates in a variation of the phase of the relative inclination vector at almost constant modulus, which implies its rotation. Further analysis of this physical interpretation is presented by the first author of this paper in his thesis.³⁶

CONCLUSIONS

The paper presents a general methodology for modeling analytically both conservative and non-conservative perturbations on the satellite relative motion. By doing so, it formalizes three new plant matrices including the effects of zonal harmonics of the geopotential up to third-order, Sun and Moon third-body and solar radiation pressure on formations in arbitrary eccentric orbits. These new models enable an analytical exploration of the relative perturbed motion geometry. In particular, two new effects have been discovered and modeled analytically. The first is the yearly circulation of the relative eccentricity vector in its phase space due to SRP for formations in near-circular orbit. The second is the rotation of the relative inclination vector in its phase space due to Sun and Moon third-body for formations in near-circular near-equatorial orbit, in occurrence of an alignment of the chief and third-bodies orbits node lines. Subsequently, the formalized analytical models are validated and their accuracy/efficiency performances assessed with respect to numerical orbit propagation. The medium/long-term accuracy provided is of at least one accurate digit, in LEO on propagation equal or longer than 10 orbits and in GPS orbit, GEO and HEO on propagation equal or longer than 100 orbits. This demonstrates the propagator capability to model the long-periodic and secular variation of the relative orbital elements under the considered perturbations. This performance, combined with the novel analytical insight, envisages the use of the new models for innovative relative orbit design and guidance in various orbits both around Earth and around other planetary bodies. Potential exploitation scenarios around Earth are the geostationary ring for on-orbit servicing and highly elliptical orbits for scientific applications as telescoping (e.g. SLAB's mDOT). Potential applications around other Solar System's planetary bodies are near-polar orbits for bi-static synthetic aperture radar mapping of the surface. In general, implementing formation-flying around other planets implies the need to account for perturbations of different intensity and variety (e.g. greater SRP around the inner planets, greater third-body around the moons of Jupiter and Saturn). Future works will further analyze the application validity and performance of the new formalized models in these scenarios of high scientific interest.

ACKNOWLEDGMENTS

The work was supported in part by the Politecnico di Milano scholarship "Theses abroad" (academic year 2015/2016) and by the King Abdulaziz City for Science and Technology (KACST).

REFERENCES

- [1] Tapley, B. D., Bettadpur, S., Watkins, M., and Reigber, C., "The gravity recovery and climate experiment: Mission overview and early results", *Geophysical Research Letters*, Vol. 31, No. 9, 2004.
- [2] Krieger, G., Moreira, A., Fiedler, H., Hajnsek, I., Werner, M., Younis, M., and Zink, M., "TanDEM-X: A satellite formation for high-resolution SAR interferometry", *IEEE Transactions on Geoscience and Remote Sensing*, Vol. 45, No. 11, 2007, pp. 3317-3341.
- [3] D'Amico, S., Ardaens, J.-S., and Larsson, R., "Spaceborne autonomous formation-flying experiment on the PRISMA mission", *Journal of Guidance, Control and Dynamics*, Vol. 35, No. 3, 2012, pp. 834-850.
- [4] Burch, J. L., Moore, T. E., Torbert, R. B., and Giles, B. L., "Magnetospheric Multiscale Overview and Science Objectives", *Space Science Reviews*, Vol. 199, No. 1-4, 2016, pp. 5-21.
- [5] Llorente, J. S., Agenjo, A., Carrascosa, C., De Negueruela, C., Mestreau-Garreau, A., Cropp, A., and Santovincenzo, A., "PROBA-3: Precise formation flying demonstration mission", *Acta Astronautica*, Vol. 82, No. 1, 2013, pp. 38-46.
- [6] Koenig, A. W., D'Amico, S., Macintosh, B., and Titus, C. J., "Formation Design Analysis for a Miniaturized Distributed Occulter/Telescope in Earth Orbit", *International Symposium on Space Flight Dynamics (ISSFD)*, 2015.
- [7] D'Amico, S., Pavone, M., Saraf, S., Alhussien, A., Al-Saud, T., Buchman, S., Byer, R., and Farhat, C., "Miniaturized Autonomous Distributed Space System for Future Science and Exploration", *Int. Workshop on Satellite Constellations and Formation Flying*, Delft, Netherlands, 2015.
- [8] Guffanti, T., and Lavagna, M., "Formation flying concept for bi-static SAR mapping of Titan surface". *26th AAS/AIAA Space Flight Mechanics Meeting*, Napa, CA, 2016.
- [9] Schweighart, S. A., and Sedwick, R. J., "High-Fidelity Linearized J_2 Model for Satellite Formation Flight", *Journal of Guidance, Control and Dynamics*, Vol. 25, No. 6, 2002, pp. 1073-1080.
- [10] Izzo, D. R., "Formation Flying Linear Modelling", *Dynamics and Control Systems and Structures in Space*, Kings College, Cambridge, 2002.
- [11] Clohessy, W. H. and Wiltshire, R. S., "Terminal Guidance System for Satellite Rendezvous", *Journal of the Aerospace Sciences*, Vol. 29, 1960, pp. 653-658.
- [12] Yamanaka, K. and Ankersen, F., "New State Transition Matrix for Relative Motion on an Arbitrary Elliptical Orbit", *Journal of guidance, control and dynamics*, Vol. 25, No. 1, 2002, pp. 60-66.
- [13] Vallado, D.A., *Fundamentals of Astrodynamics and Applications*, Space Technology Library, 2013.
- [14] Gim, D.-W., and Alfriend, K. T., "State transition matrix of relative motion for the perturbed noncircular reference orbit", *Journal of Guidance, Control and Dynamics*, Vol. 26, No. 6, 2003, pp. 956-971.
- [15] Gim, D., and Alfriend, K., "Criteria for Best Configuration and Sub-optimal Reconfiguration for MMS Mission", *AAS Spaceflight Mechanics Meeting*, Maui, HI, 2004.
- [16] Roscoe, C. W., Westphal, J. J., Griesbach, J. D., and Schaub, H., "Formation Establishment and Reconfiguration Using Differential Elements in J_2 -Perturbed Orbits", *Journal of Guidance, Control and Dynamics*, Vol. 38, No. 9, 2015, pp. 1725-1740.
- [17] Gim, D.-W., and Alfriend, K. T., "Satellite relative motion using differential equinoctial elements", *Celestial Mechanics and Dynamical Astronomy*, Vol. 92, No. 4, 2005, pp. 295-336.
- [18] Mahajan, B., Vadali, S. R., and Alfriend, K. T., "Analytic Solution for Satellite Relative Motion with Zonal Gravity Perturbations", No. 15-705, *AAS/AIAA Astrodynamics Specialist Conference*, Vail, August 2015.
- [19] Mahajan, B., Vadali, S. R., and Alfriend, K. T., "Analytic Solution for the Satellite Relative Motion: The Complete Zonal Gravitational Problem", *Proceedings of the 26th AAS/AIAA Space Flight Mechanics Meeting*, Napa, CA, 2016.
- [20] D'Amico, S., *Autonomous formation flying in low earth orbit*, TU Delft, Delft University of Technology, 2010.
- [21] Gaias, G., D'Amico, S., and Ardaens, J.-S., "Generalised multi-impulsive manoeuvres for optimum spacecraft rendezvous in near-circular orbit", *International Journal of Space Science and Engineering*, Vol. 3, No. 1, 2015, pp. 68-88.
- [22] Gaias, G., Ardaens, J.-S., and Montenbruck, O., "Model of J_2 perturbed satellite relative motion with time-varying differential drag", *Celestial Mechanics and Dynamical Astronomy*, Vol. 123, No. 4, 2015, pp. 411-433.

- [23] Montenbruck, O., Kirschner, M., D’Amico, S., and Bettadpur, S., ”E/I-vector separation for safe switching of the GRACE formation”, *Aerospace Science and Technology*, Vol. 10, No. 7, 2006, pp. 628-635.
- [24] Montenbruck, O., Kahle, R., D’Amico, S., and Ardaens, J.-S., ”Navigation and control of the TanDEM-X formation”, *The Journal of the Astronautical Sciences*, Vol. 56, No. 3, 2008, pp. 341-357.
- [25] Gaias, G., Ardaens, J.-S., and D’Amico, S., ”The autonomous vision approach navigation and target identification (AVANTI) experiment: objectives and design”, *9th International ESA Conference on Guidance, Navigation & Control Systems*, Porto, Portugal, 2014.
- [26] Koenig, A., Guffanti, T., and D’Amico, S., ”New State Transition Matrices for Relative Motion of Spacecraft Formations in Perturbed Orbits”, *AIAA Space and Astronautics Form and Exposition*, SPACE 2016, 13-16 September, 2016, Long Beach Convention Center, California, United States (2016).
- [27] Roscoe, C.W.T., Vadali, S.R. and Alfriend, K.T., ”Third-body perturbation effects on satellite formations”, *The Journal of the Astronautical Sciences*, 2013.
- [28] Spiridonova, S., and Kahle, R., ”Relative orbit dynamics in near-geostationary orbit”, *International Symposium on Space Flight Dynamics*, 2015.
- [29] Spiridonova, S., ”Formation dynamics in geostationary ring”, *Celestial Mechanics and Dynamical Astronomy*, Springer, 2016.
- [30] Sullivan, J., Grimberg, S., and D’Amico, S., ”A Comprehensive Survey and Assessment of Spacecraft Relative Motion Dynamics Models”, *Journal of Guidance, Control, and Dynamics*, 2017. (Accepted)
- [31] Liu, J.J.F., ”Satellite Motion about an Oblate Earth”, *AIAA Journal*, Vol. 12, No. 11, Nov. 1974, pp.1511-1516.
- [32] Liu, J.J.F., and Alford, R.L., ”Semianalytic theory for a close-Earth artificial satellite”, *Journal of Guidance and Control*, 1980.
- [33] Cook, G.E., ”Luni-solar perturbations of the orbit of an Earth satellite”, *The Geophysical Journal of the Royal Astronomical Society*, 1962.
- [34] Chao, C.C., *Applied Orbit Perturbation and Maintenance*, The Aerospace Press, 2005.
- [35] Montenbruck, O., and Gill, E., *Satellite orbits: Models, Methods and Applications*, Springer Verlag, 2000.
- [36] Guffanti, T., *A Semianalytical Study on the Satellite Relative Perturbed Motion Modeling in Relative Orbital Elements*, Master Thesis, Politecnico di Milano, July, 2016.

APPENDIX

ABSOLUTE DYNAMIC MODELS

Geopotential (J_2 and J_3)

The mean orbital elements variations due to J_2 and J_3 formalized by Liu and Alford^{31,32} are

$$\begin{aligned}
\left\langle \frac{da}{dt} \right\rangle &= 0 \\
\left\langle \frac{de}{dt} \right\rangle &= -\frac{3}{8}nJ_3\left(\frac{R_E}{p}\right)^3 \sin(i)[4 - 5\sin^2(i)](1 - e^2) \cos(\omega) \\
\left\langle \frac{di}{dt} \right\rangle &= \frac{3}{8}nJ_3\left(\frac{R_E}{p}\right)^3 \cos(i)[4 - 5\sin^2(i)]e \cos(\omega) \\
\left\langle \frac{d\Omega}{dt} \right\rangle &= -\frac{3}{2}nJ_2\left(\frac{R_E}{p}\right)^2 \cos(i) - \frac{3}{8}nJ_3\left(\frac{R_E}{p}\right)^3 [15\sin^2(i) - 4]e \cot(i) \sin(w) \\
\left\langle \frac{d\omega}{dt} \right\rangle &= \frac{3}{4}nJ_2\left(\frac{R_E}{p}\right)^2 [4 - 5\sin^2(i)] + \\
&+ \frac{3}{8}nJ_3\left(\frac{R_E}{p}\right)^3 \left\{ [4 - 5\sin^2(i)] \frac{\sin^2(i) - e^2 \cos^2(i)}{e \sin(i)} + 2 \sin(i)[13 - 15\sin^2(i)]e \right\} \sin(w) \\
\left\langle \frac{dM}{dt} \right\rangle &= \frac{3}{2}nJ_2\left(\frac{R_E}{p}\right)^2 \left[1 - \frac{3}{2}\sin^2(i)\right] \sqrt{1 - e^2} + \\
&- \frac{3}{8}nJ_3\left(\frac{R_E}{p}\right)^3 \sin(i)[4 - 5\sin^2(i)] \frac{1 - 4e^2}{e} \sqrt{1 - e^2} \sin(w)
\end{aligned} \tag{38}$$

Where R_E is the Earth equatorial radius, J_2 and J_3 are the second and third-order zonal geopotential coefficients, n is the satellite mean motion and p is the satellite orbit semilatus rectum.

Sun and Moon Third-body

The mean orbital elements variations due to Sun and Moon third-body effect formalized by Cook³³ and also presented by Vallado¹³ are

$$\begin{aligned}
\left\langle \frac{da}{dt} \right\rangle &= 0 \\
\left\langle \frac{de}{dt} \right\rangle &= 0 \\
\left\langle \frac{di}{dt} \right\rangle &= \frac{3\mu_3 C}{4r_3^3 n \sqrt{1-e^2}} \left\{ A \left[2 + 3e^2 + 5e^2 \cos(2\omega) \right] + 5Be^2 \sin(2\omega) \right\} \\
\left\langle \frac{d\Omega}{dt} \right\rangle &= \frac{3\mu_3 C}{4r_3^3 n \sqrt{1-e^2} \sin(i)} \left\{ 5Ae^2 \sin(2\omega) + B \left[2 + 3e^2 - 5e^2 \cos(2\omega) \right] \right\} \\
\left\langle \frac{d\omega}{dt} \right\rangle &= -\frac{3\mu_3 C \cos(i)}{4r_3^3 n \sqrt{1-e^2} \sin(i)} \left\{ 5Ae^2 \sin(2\omega) + B \left[2 + 3e^2 - 5e^2 \cos(2\omega) \right] \right\}
\end{aligned} \tag{39}$$

where subscript "3" indicates quantities related to the third-body, μ_3 is the third-body standard gravitational parameter, r_3 is the third-body distance from the Earth center and n is the satellite mean motion. The direction cosines for the third-body are

$$\begin{aligned}
A &= \cos(\Omega - \Omega_3) \cos(u_3) + \cos(i_3) \sin(u_3) \sin(\Omega - \Omega_3) \\
B &= \cos(i) [-\sin(\Omega - \Omega_3) \cos(u_3) + \cos(i_3) \sin(u_3) \cos(\Omega - \Omega_3)] + \sin(i) \sin(i_3) \sin(u_3) \\
C &= \sin(i) [\cos(u_3) \sin(\Omega - \Omega_3) - \cos(i_3) \sin(u_3) \cos(\Omega - \Omega_3)] + \cos(i) \sin(i_3) \sin(u_3)
\end{aligned} \tag{40}$$

Solar Radiation Pressure

The mean orbital elements variations due to SRP, neglecting the effects of eclipses, for a satellite in Sun-light during the entire orbit, formalized by Cook³³ and then presented by Vallado¹³ are

$$\begin{aligned}
\left\langle \frac{da}{dt} \right\rangle &= 0 \\
\left\langle \frac{de}{dt} \right\rangle &= \frac{3\sqrt{1-e^2}}{2na} S_p \\
\left\langle \frac{di}{dt} \right\rangle &= -\frac{3eW \cos(\omega)}{2na\sqrt{1-e^2}} \\
\left\langle \frac{d\Omega}{dt} \right\rangle &= -\frac{3eW \sin(\omega)}{2na\sqrt{1-e^2} \sin(i)} \\
\left\langle \frac{d\omega}{dt} \right\rangle &= -\frac{3\sqrt{1-e^2}}{2nae} R_p - \frac{d\Omega}{dt} \cos(i) \\
\left\langle \frac{dM}{dt} \right\rangle &= \frac{9eR_p}{2na} - \sqrt{1-e^2} \left(\frac{d\omega}{dt} + \frac{d\Omega}{dt} \cos(i) \right)
\end{aligned} \tag{41}$$

Where the radial (R_p), transverse (S_p) and normal (W) components of the disturbing SRP force evaluated at the perigee as if the perigee is in Sun-light are

$$\begin{aligned}
R_p &= F_{srp} B_{srp} \cdot \left\{ \left[\cos^2 \left(\frac{\epsilon}{2} \right) \cos(\omega + \Omega - \lambda_s) + \sin^2 \left(\frac{\epsilon}{2} \right) \cos(\omega + \Omega + \lambda_s) \right] \cos^2 \left(\frac{i}{2} \right) + \left[\cos^2 \left(\frac{\epsilon}{2} \right) \cdot \right. \right. \\
&\quad \left. \cdot \cos(\omega - \Omega + \lambda_s) + \sin^2 \left(\frac{\epsilon}{2} \right) \cos(\omega - \Omega - \lambda_s) \right] \sin^2 \left(\frac{i}{2} \right) + \frac{1}{2} [\cos(\omega - \lambda_s) - \cos(\omega + \lambda_s)] \sin(i) \sin(\epsilon) \right\}
\end{aligned} \tag{42}$$

$$\begin{aligned}
S_p &= -F_{srp} B_{srp} \cdot \left\{ \left[\cos^2 \left(\frac{\epsilon}{2} \right) \sin(\omega + \Omega - \lambda_s) + \sin^2 \left(\frac{\epsilon}{2} \right) \sin(\omega + \Omega + \lambda_s) \right] \cos^2 \left(\frac{i}{2} \right) + \left[\cos^2 \left(\frac{\epsilon}{2} \right) \cdot \right. \right. \\
&\quad \left. \cdot \sin(\omega - \Omega + \lambda_s) + \sin^2 \left(\frac{\epsilon}{2} \right) \sin(\omega - \Omega - \lambda_s) \right] \sin^2 \left(\frac{i}{2} \right) - \frac{1}{2} [\sin(\omega + \lambda_s) - \sin(\omega - \lambda_s)] \sin(i) \sin(\epsilon) \right\}
\end{aligned} \tag{43}$$

$$\begin{aligned}
W \sin(\omega) &= -\frac{F_{srp}}{2} B_{srp} \cdot \left\{ [\cos(\omega + \Omega - \lambda_s) - \cos(\omega - \Omega + \lambda_s)] \sin(i) \cos^2 \left(\frac{\epsilon}{2} \right) + [\cos(\omega + \Omega + \lambda_s) + \right. \\
&\quad \left. - \cos(\omega - \Omega - \lambda_s)] \sin(i) \sin^2 \left(\frac{\epsilon}{2} \right) + [\cos(\omega + \lambda_s) - \cos(\omega - \lambda_s)] \cos(i) \sin(\epsilon) \right\} \\
W \cos(\omega) &= \frac{F_{srp}}{2} B_{srp} \cdot \left\{ [\sin(\omega + \Omega - \lambda_s) - \sin(\omega - \Omega + \lambda_s)] \sin(i) \cos^2 \left(\frac{\epsilon}{2} \right) + [\sin(\omega + \Omega + \lambda_s) + \right. \\
&\quad \left. - \sin(\omega - \Omega - \lambda_s)] \sin(i) \sin^2 \left(\frac{\epsilon}{2} \right) + [\sin(\omega + \lambda_s) - \sin(\omega - \lambda_s)] \cos(i) \sin(\epsilon) \right\}
\end{aligned} \tag{44}$$

with $F_{srp} = \frac{P_{Sun}}{c} \left(\frac{a_{Sun}}{r_{Sun}} \right)^2$, $\frac{P_{Sun}}{c} = \frac{1353W/m^2}{3 \cdot 10^8 m/s}$, $\frac{a_{Sun}}{r_{Sun}} \approx 1$ or as a function of time as in Chao,³⁴ $\epsilon = 23.44^\circ$. λ_s is the ecliptic longitude of the Sun and $B_{srp} = \frac{C_r A_{srp}}{m}$ is the satellite ballistic coefficient related to SRP.

PLANT MATRICES

In the following, $\eta = \sqrt{1 - \|e\|^2}$ and $\sin(\cdot) = s$. and $\cos(\cdot) = c$.

J₂ Plant Matrix

$$\mathbf{A}_{geopJ_2} = \kappa_{J_2} \cdot \begin{bmatrix} 0 & 0 & 0 & 0 & 0 & 0 & 0 \\ -\frac{7}{2}EP & 0 & e_x GFP & e_y GFP & -FS & 0 & 0 \\ \frac{7}{2}e_y Q & 0 & -4e_x e_y GQ & -(1 + 4Ge_y^2)Q & 5e_y S & 0 & 0 \\ -\frac{7}{2}e_x Q & 0 & (1 + 4Ge_x^2)Q & 4e_x e_y GQ & -5e_x S & 0 & 0 \\ 0 & 0 & 0 & 0 & 0 & 0 & 0 \\ \frac{7}{2}S & 0 & -4e_x GS & -4e_y GS & 2T & 0 & 0 \\ 0 & 0 & 0 & 0 & 0 & 0 & 0 \end{bmatrix} \quad (45)$$

J₃ Plant Matrix

$$\mathbf{A}_{geopJ_3} = \kappa_{J_3} \cdot \begin{bmatrix} 0 & 0 & 0 & 0 & 0 & 0 & 0 \\ \frac{9}{2}e_y ZJ & 0 & -6e_x e_y GZJ & -(6e_y^2 + \eta^2)GZJ & -e_y c_i H & 0 & 0 \\ \frac{9}{2}\mathcal{T} & 0 & -6e_x G(\mathcal{T} - \frac{\eta^2}{3}s_i Q) & -6e_y G[\mathcal{T} + \frac{\eta^2}{3}(-ZQ + Y)] & -[(1 - e_x^2)U + e_y^2 W] & 0 & 0 \\ -\frac{9}{2}e_x e_y K & 0 & (6e_x^2 e_y + \eta^2 e_y)GK & (6e_x e_y^2 + \eta^2 e_x)GK & e_x e_y (U + W) & 0 & 0 \\ -\frac{9}{2}e_x c_i Q & 0 & (6e_x^2 + \eta^2)Gc_i Q & 6e_x e_y Gc_i Q & -e_x (s_i Q + 5Sc_i) & 0 & 0 \\ \frac{9}{2}e_y c_i J & 0 & -6e_x e_y Gc_i J & -(6e_y^2 + \eta^2)Gc_i J & -e_y s_i H & 0 & 0 \\ 0 & 0 & 0 & 0 & 0 & 0 & 0 \end{bmatrix} \quad (46)$$

Terms of the J₂ and J₃ Plant Matrices

$$\begin{aligned} \gamma_{J_2} &= \frac{3}{4} J_2 R_E^2 \sqrt{\mu} & \kappa_{J_2} &= \frac{\gamma_{J_2}}{a^{\frac{7}{2}} \eta^4} & \gamma_{J_3} &= \frac{3}{8} J_3 R_E^3 \sqrt{\mu} & \kappa_{J_3} &= \frac{\gamma_{J_3}}{a^{\frac{9}{2}} \eta^6} \\ F &= 4 + 3\eta & E &= 1 + \eta & G &= \frac{1}{\eta^2} & Q &= 5c_i^2 - 1 & P &= 3c_i^2 - 1 \\ J &= 11 - 15c_i^2 & L &= 15c_i^2 - 2 & S &= s_{2i} & T &= s_i^2 & Z &= \cot(i)c_i \\ Y &= 2s_i L & H &= \frac{30c_i^2 s_i^2 - J}{s_i^2} & U &= c_i Q - 5Ss_i & W &= \frac{Ss_i + c_i^3}{s_i^2} Q + 40c_i^3 - (4c_i + 30Ss_i) \\ K &= Q(s_i - Z) + Y & \mathcal{T} &= (1 - e_x^2)s_i Q + e_y^2(-ZQ + Y) \end{aligned} \quad (47)$$

(48)

$$\mathbf{A}_{3^{rd}b} = k_{3^{rd}b} \cdot \begin{bmatrix} 0 & 0 & 0 & 0 & 0 & 0 & 0 \\ 0 & 0 & 0 & 0 & 0 & 0 & 0 \\ \frac{3}{2}((F\mathcal{T}_1 + E_2\mathcal{T}_2)\frac{e_y}{t_i} & 0 & (\mathcal{T}_1\mathcal{T}_7 + \mathcal{T}_2\mathcal{T}_5)\frac{e_y}{t_i} & (\mathcal{T}_1\mathcal{T}_8 + \mathcal{T}_2\mathcal{T}_4)\frac{e_y}{t_i} & \mathcal{T}_{15}\frac{e_y}{t_i} & -\mathcal{T}_{16} & \frac{3}{2}((F\mathcal{T}_{13} + E_2\mathcal{T}_{14})\frac{e_y}{t_i}) \\ -\frac{3}{2}((F\mathcal{T}_1 + E_2\mathcal{T}_2)\frac{e_x}{t_i} & 0 & -(\mathcal{T}_1\mathcal{T}_7 + \mathcal{T}_2\mathcal{T}_5)\frac{e_x}{t_i} - \frac{\mathcal{T}_{15}}{t_i} & -(\mathcal{T}_1\mathcal{T}_8 + \mathcal{T}_2\mathcal{T}_4)\frac{e_x}{t_i} & -\mathcal{T}_{17}\frac{e_x}{t_i} & \mathcal{T}_{15}e_y & -\frac{3}{2}((F\mathcal{T}_{13} + E_2\mathcal{T}_{14})\frac{e_x}{t_i}) \\ \frac{3}{2}(E_1\mathcal{T}_1 + F\mathcal{T}_2) & 0 & \mathcal{T}_1\mathcal{T}_3 + \mathcal{T}_2\mathcal{T}_7 & \mathcal{T}_1\mathcal{T}_6 + \mathcal{T}_2\mathcal{T}_8 & E_1\mathcal{T}_{11} + F\mathcal{T}_{12} & E_1\mathcal{T}_{13} + F\mathcal{T}_{14} & \frac{3}{2}(E_1\mathcal{T}_{13} + F\mathcal{T}_{14}) \\ \frac{3}{2}(F\mathcal{T}_1 + E_2\mathcal{T}_2) & 0 & \mathcal{T}_1\mathcal{T}_7 + \mathcal{T}_2\mathcal{T}_5 & \mathcal{T}_1\mathcal{T}_8 + \mathcal{T}_2\mathcal{T}_4 & \mathcal{T}_{17} & F(\mathcal{T}_{13} + \mathcal{T}_{10}) + E_2\mathcal{T}_{14} + E_1\mathcal{T}_9 & 0 \\ 0 & 0 & 0 & 0 & 0 & 0 & 0 \end{bmatrix}.$$

Solar Radiation Pressure Plant Matrix

(49)

$$\mathbf{A}_{srp} = k_{srp} \cdot \begin{bmatrix} 0 & 0 & 0 & 0 & 0 & 0 & 0 \\ -e_x \mathcal{T}_1 + e_y \mathcal{T}_2 & 0 & -2\mathcal{T}_1 & 0 & (-2 + \frac{1}{\eta}) e_y \mathcal{T}_3 & 0 & 0 \\ \frac{\eta}{2} \mathcal{T}_2 + \frac{e_y}{2\eta} \mathcal{T}_4 & 0 & -\frac{e_x}{\eta} \mathcal{T}_2 + \frac{e_y}{\eta^3} \mathcal{T}_4 & -\frac{e_x}{\eta} \mathcal{T}_2 + (\frac{2e_y}{\eta} + \frac{e_y}{\eta^3}) \mathcal{T}_4 & -\eta \mathcal{T}_3 - \frac{e_y}{\eta} \mathcal{T}_5 & \frac{2(e_x \mathcal{T}_6 + e_y \mathcal{T}_1)}{\eta^2 + e_y^2} \frac{\cot(i)}{s_i} \mathcal{T}_1 & -\frac{2}{B_{srp}} (e_x \mathcal{T}_1 - e_y \mathcal{T}_2) - \frac{e_y}{\eta B_{srp}} \mathcal{T}_4 \\ \frac{\eta}{2} \mathcal{T}_1 - \frac{e_x e_y}{2\eta} \mathcal{T}_4 & 0 & -\frac{e_x}{\eta} \mathcal{T}_1 - (\frac{e_y}{\eta} + \frac{e_y e_x}{\eta^3}) \mathcal{T}_4 & -\frac{e_y}{\eta} \mathcal{T}_1 - (\frac{e_x}{\eta} + \frac{e_y^2}{\eta^3}) \mathcal{T}_4 & + \frac{e_x e_y}{\eta} \mathcal{T}_5 & -\frac{\eta}{s_i^2} \mathcal{T}_6 - \frac{e_x e_y \cot(i)}{\eta} \mathcal{T}_1 & \frac{\eta}{B_{srp}} \mathcal{T}_2 + \frac{e_y}{\eta B_{srp}} \mathcal{T}_4 \\ \frac{e_x}{2\eta} \mathcal{T}_3 & 0 & (\frac{1}{\eta} + \frac{e_y^2}{\eta^3}) \mathcal{T}_3 & \frac{e_x e_y}{\eta^3} \mathcal{T}_3 & \frac{e_x}{\eta} \mathcal{T}_2 & -\frac{\eta}{s_i^2} \mathcal{T}_6 - \frac{e_x e_y \cot(i)}{\eta} \mathcal{T}_1 & \frac{e_x}{\eta B_{srp}} \mathcal{T}_3 \\ \frac{e_y}{2\eta} \mathcal{T}_3 & 0 & \frac{e_x e_y}{\eta^3} \mathcal{T}_3 & (\frac{1}{\eta} + \frac{e_y^2}{\eta^3}) \mathcal{T}_3 & -\frac{e_y}{\eta} s_i^2 \mathcal{T}_5 & \frac{e_y}{\eta} \mathcal{T}_1 + \frac{e_x}{\eta} \mathcal{T}_4 & \frac{e_y}{\eta B_{srp}} \mathcal{T}_3 \\ 0 & 0 & 0 & 0 & 0 & 0 & 0 \end{bmatrix}$$

Terms of the Sun and Moon Third-body Plant Matrix

$$\begin{aligned}
\gamma_{3^{rd}b} &= \frac{3\mu_3}{4r_3^3\sqrt{\mu}} & \kappa_{3^{rd}b} &= \frac{\gamma_{3^{rd}b}\sqrt{a^3}}{\eta} & t_i &= \tan(i) \\
B_{\delta i_x} &= \frac{\partial B}{\partial \delta i_x} = -s_i[-\sin(\Omega - \Omega_3)c_{u_3} + c_{i_3}s_{u_3}\cos(\Omega - \Omega_3)] + c_i s_{i_3}s_{u_3} \\
C_{\delta i_x} &= \frac{\partial C}{\partial \delta i_x} = c_i[c_{u_3}\sin(\Omega - \Omega_3) - c_{i_3}s_{u_3}\cos(\Omega - \Omega_3)] - s_i s_{i_3}s_{u_3} \\
A_{\delta i_y} &= \frac{\partial A}{\partial \delta i_y} = -\frac{\sin(\Omega - \Omega_3)}{s_i}c_{u_3} + c_{i_3}s_{u_3}\frac{\cos(\Omega - \Omega_3)}{s_i} \\
B_{\delta i_y} &= \frac{\partial B}{\partial \delta i_y} = c_i\left[-\frac{\cos(\Omega - \Omega_3)}{s_i}c_{u_3} - c_{i_3}s_{u_3}\frac{\sin(\Omega - \Omega_3)}{s_i}\right] \\
C_{\delta i_y} &= \frac{\partial C}{\partial \delta i_y} = s_i\left[c_{u_3}\frac{\cos(\Omega - \Omega_3)}{s_i} + c_{i_3}s_{u_3}\frac{\sin(\Omega - \Omega_3)}{s_i}\right] \\
E_1 &= 2 + 3e^2 + 5e_x^2 - 5e_y^2 & E_2 &= 2 + 3e^2 - 5e_x^2 + 5e_y^2 & F &= 10e_x e_y \\
\mathcal{T}_1 &= CA & \mathcal{T}_2 &= CB \\
\mathcal{T}_3 &= \frac{e_x}{\eta^2}E_1 + 16e_x & \mathcal{T}_4 &= \frac{e_y}{\eta^2}E_2 + 16e_y & \mathcal{T}_5 &= \frac{e_x}{\eta^2}E_2 - 4e_x \\
\mathcal{T}_6 &= \frac{e_y}{\eta^2}E_1 - 4e_y & \mathcal{T}_7 &= \frac{e_x}{\eta^2}F + 10e_y & \mathcal{T}_8 &= \frac{e_y}{\eta^2}F + 10e_x \\
\mathcal{T}_9 &= \frac{\mathcal{T}_1}{t_i} & \mathcal{T}_{10} &= \frac{\mathcal{T}_2}{t_i} \\
\mathcal{T}_{11} &= C_{\delta i_x}A & \mathcal{T}_{12} &= C_{\delta i_x}B + CB_{\delta i_x} & \mathcal{T}_{13} &= C_{\delta i_y}A + CA_{\delta i_y} \\
\mathcal{T}_{14} &= C_{\delta i_y}B + CB_{\delta i_y} & \mathcal{T}_{15} &= FCA + E_2CB & \mathcal{T}_{16} &= FCB + E_1CA \\
\mathcal{T}_{17} &= F(\mathcal{T}_{11} - \mathcal{T}_9) + E_2(\mathcal{T}_{12} - \mathcal{T}_{10})
\end{aligned} \tag{50}$$

Terms of the Solar Radiation Pressure Plant Matrix

$$\begin{aligned}
\gamma_{srp} &= \frac{3F_{srp}}{2\sqrt{\mu}} & \kappa_{srp} &= \gamma_{srp}B_{srp}\sqrt{a} & y_s &= s_{\lambda_s}c_i & z_s &= s_{\lambda_s}s_i \\
X_{s_1} &= \cos(\Omega - \lambda_s) & Y_{s_1} &= \sin(\Omega - \lambda_s)c_i & Z_{s_1} &= \sin(\Omega - \lambda_s)s_i \\
X_{s_2} &= \cos(\Omega + \lambda_s) & Y_{s_2} &= \sin(\Omega + \lambda_s)c_i & Z_{s_2} &= \sin(\Omega + \lambda_s)s_i \\
\mathcal{T}_1 &= c_{\frac{\epsilon}{2}}^2 X_{s_1} + s_{\frac{\epsilon}{2}}^2 X_{s_2} & \mathcal{T}_2 &= c_{\frac{\epsilon}{2}}^2 Y_{s_1} + s_{\frac{\epsilon}{2}}^2 Y_{s_2} - s_{\epsilon}z_s & \mathcal{T}_3 &= c_{\frac{\epsilon}{2}}^2 Z_{s_1} + s_{\frac{\epsilon}{2}}^2 Z_{s_2} + s_{\epsilon}y_s \\
\mathcal{T}_4 &= c_{\frac{\epsilon}{2}}^2 Y_{s_1} + s_{\frac{\epsilon}{2}}^2 Y_{s_2} + s_{\epsilon}y_s \cot(i) & \mathcal{T}_5 &= c_{\frac{\epsilon}{2}}^2 Z_{s_1} + s_{\frac{\epsilon}{2}}^2 Z_{s_2} + s_{\epsilon}y_s \frac{2s_i^2 + c_i^2}{s_i^2} & \mathcal{T}_6 &= c_{\frac{\epsilon}{2}}^2 Z_{s_1} + s_{\frac{\epsilon}{2}}^2 Z_{s_2}
\end{aligned} \tag{51}$$

VALIDATION PLOTS

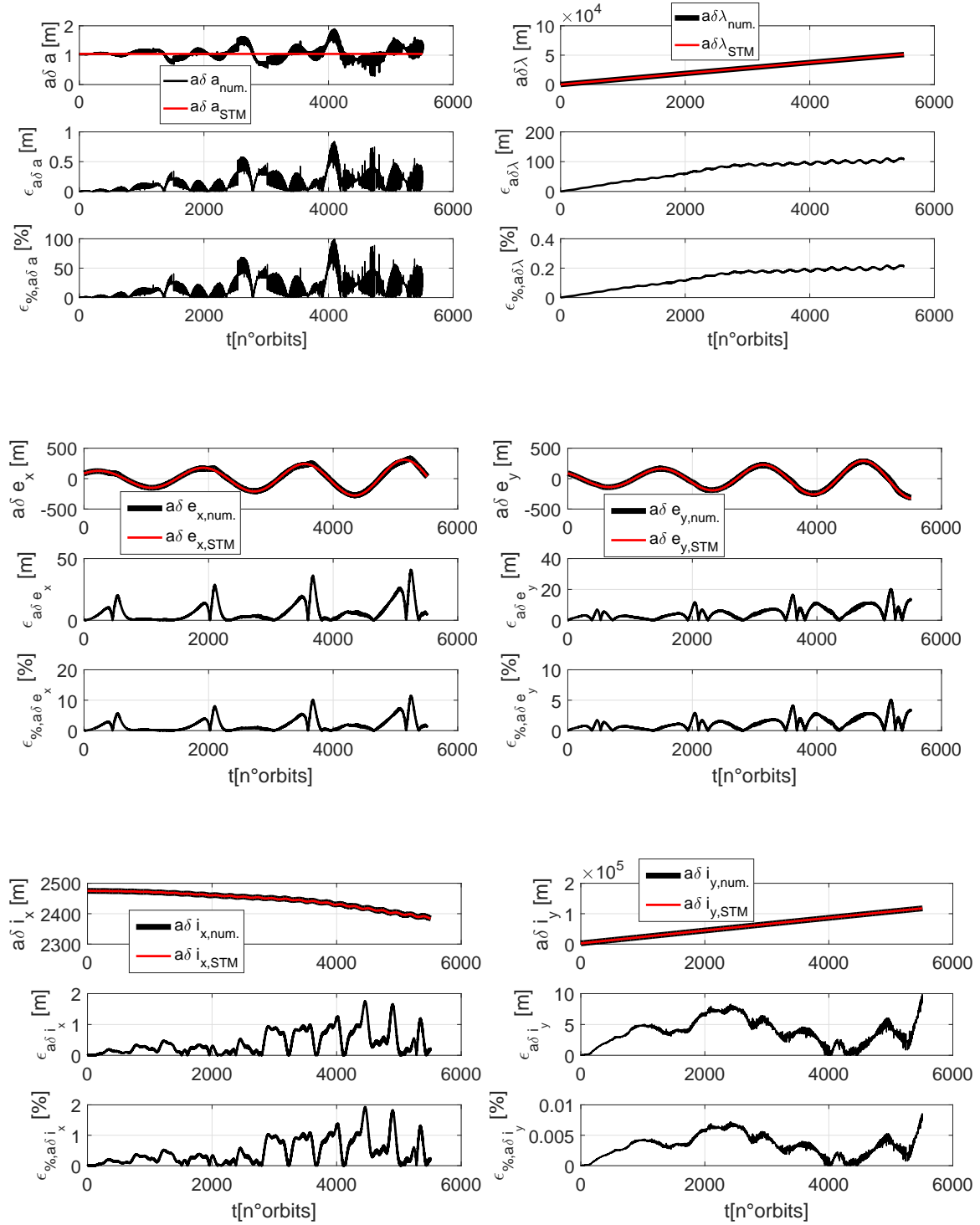


Figure 9: LEO formation, perturbed by J_2 , J_3 , SRP and Sun/Moon third-body, 1year of propagation.

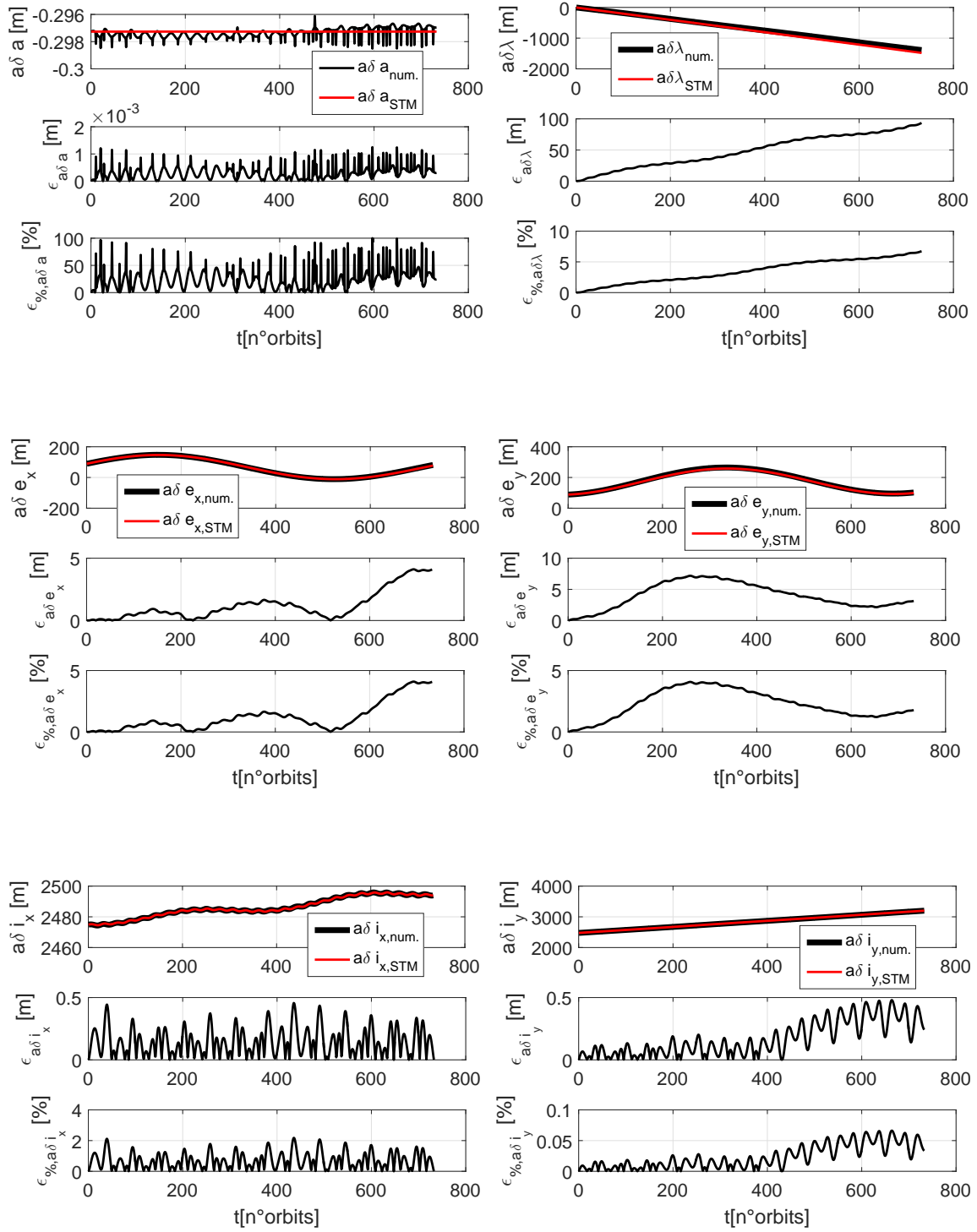


Figure 10: GPS orbit formation, perturbed by J_2 , J_3 , SRP and Sun/Moon third-body, 1year of propagation.

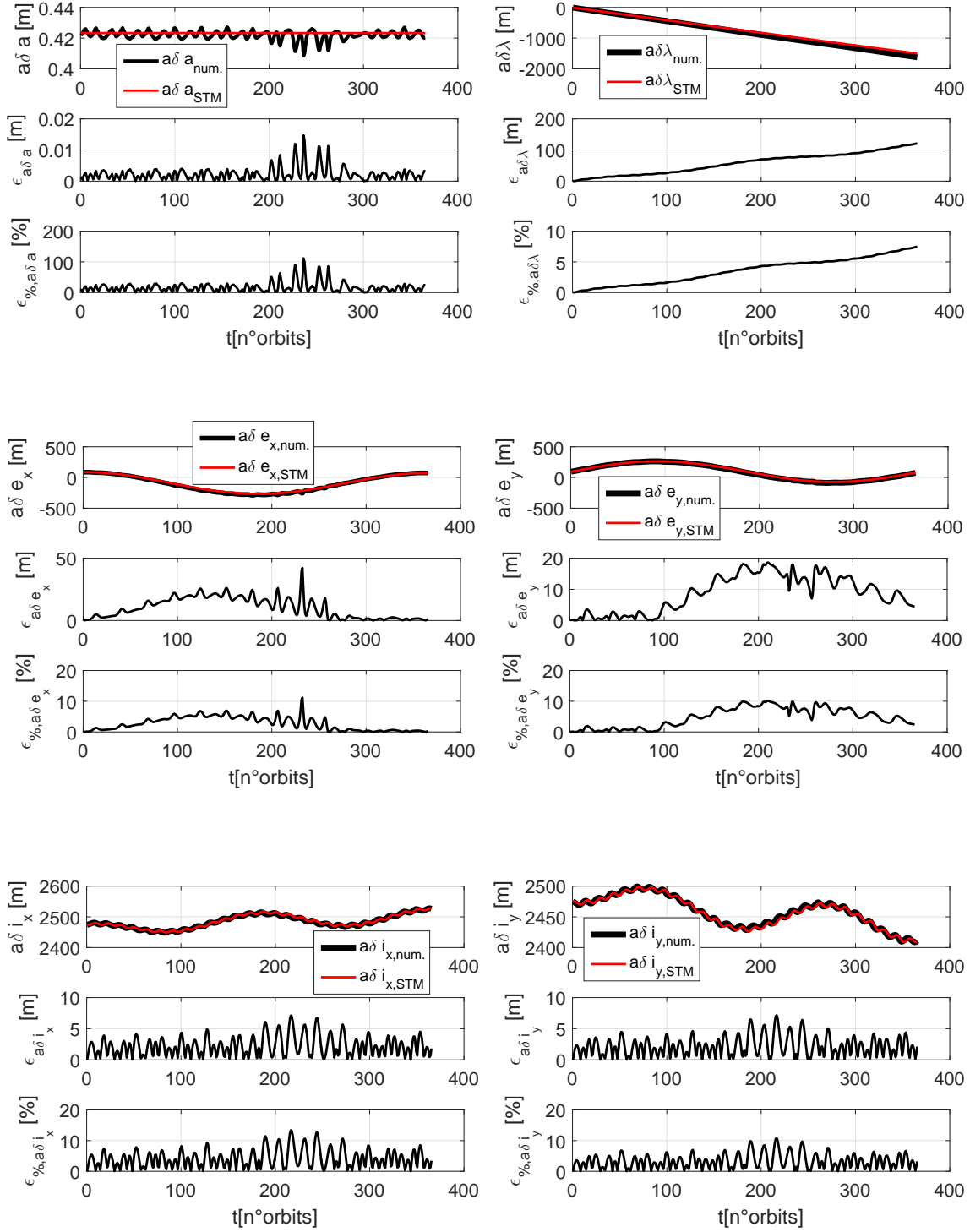


Figure 11: GEO formation, perturbed by J_2 , J_3 , SRP and Sun/Moon third-body, 1year of propagation.

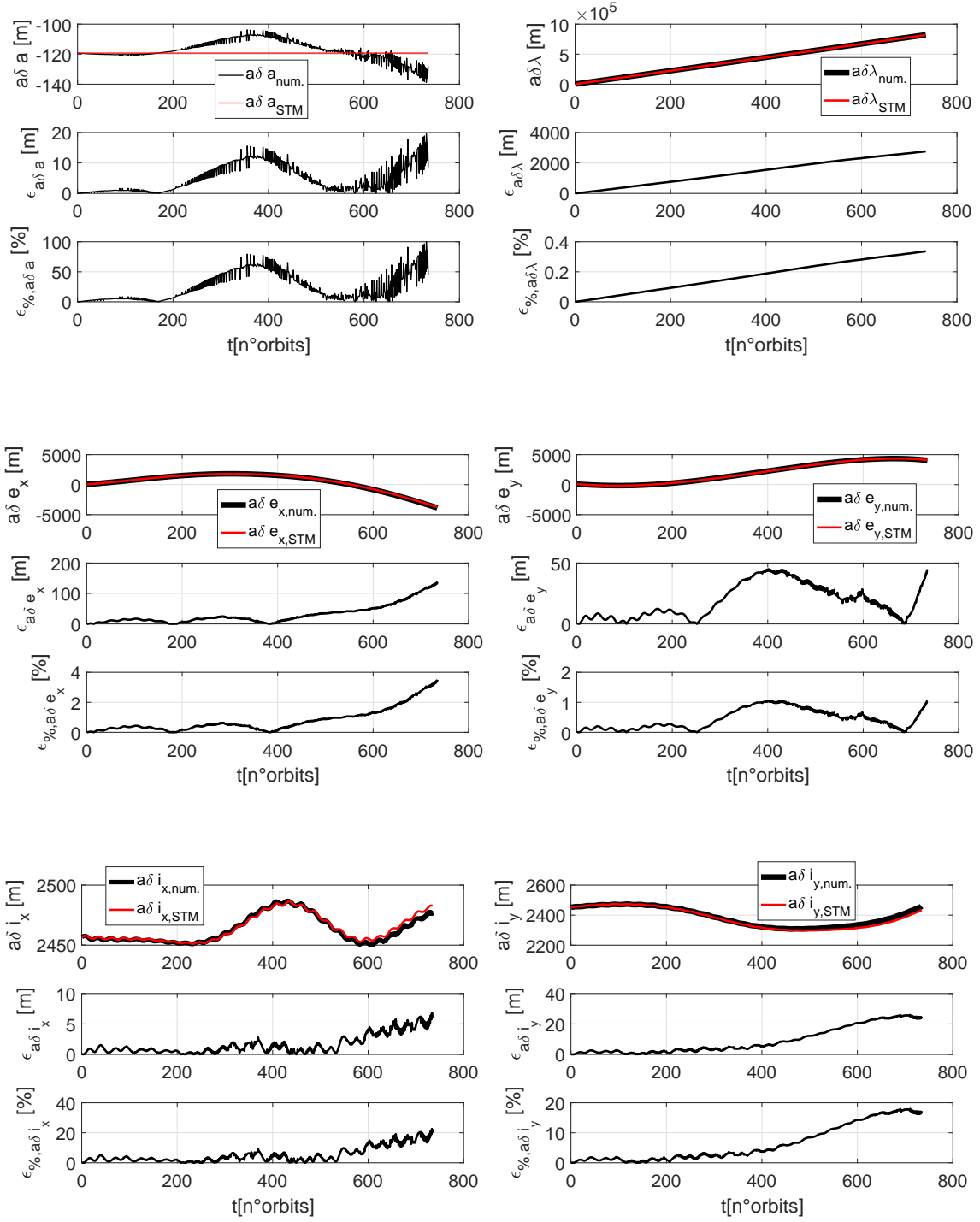


Figure 12: HEO formation, perturbed by J_2 , J_3 , SRP and Sun/Moon third-body, 1year of propagation.